https://doi.org/10.5194/se-2021-45
Preprint. Discussion started: 21 April 2021

Solid Earth Discussions

Investigating Spatial Heterogeneity within Fracture Networks using Hierarchical Clustering and Graph Distance Metrics

Rahul Prabhakaran[1,2], Giovanni Bertotti[1], Janos Urai[3], and David Smeulders[2]

[1]Department of Geoscience and Engineering, Delft University of Technology, Delft, the Netherlands
[2]Department of Mechanical Engineering, Eindhoven University of Technology, the Netherlands
[3]Structural Geology, Tectonics and Geomechanics, RWTH Aachen University, Aachen, Germany

Correspondence: Rahul Prabhakaran (r.prabhakaran@tudelft.nl)

Abstract. We investigate the spatial variation of 2D fracture networks digitized from the well-known Lilstock limestone pavements, Bristol Channel, UK. By treating fracture networks as spatial graphs, we utilize a novel approach combining graph similarity measures and hierarchical clustering to identify spatial clusters within fracture networks and quantify spatial variation. We use four graph similarity measures: fingerprint distance, D-measure, NetLSD, and portrait divergence to compare fracture graphs. The technique takes into account both topological relationship and geometry of the networks and is applied to three large fractured regions consisting of nearly 300,000 fractures spread over 14,200 sq.m. The results indicates presence of spatial clusters within fracture networks with that vary gradually over distances of tens of metres. One region is not influenced by faulting but still displays variation in background fracturing. Variation in fracture development in the other two regions are interpreted to be primarily influenced by proximity to faults that gradually gives way to background fracturing. Comparative analysis of the graph similarity-derived clusters with fracture persistence measures indicate that there is a general correspondence between patterns; however, additional variations are highlighted that is not obvious from fracture intensity and density plots. The proposed method provides a quantitative way to identify spatial variations in fracture networks which can be used to guide stochastic and geostatistical approaches to fracture network modelling.

1 Introduction

Fracture networks in rocks develop due to loading paths that vary over geological time-scale (Laubach et al., 2019). The evolution of the network exhibits characteristics of a complex system. There is feedback between the evolving spatial structure and the rock substrate in which the networks are positioned (Laubach et al., 2018). The resulting spatial arrangement that emerges after cumulative network evolution is of considerable interest as it influences flow, transport, and geomechanical stability in multiple anthropogenic subsurface applications such as geothermal energy (Vidal et al., 2017), nuclear waste disposal (Wang and Hudson, 2015), aquifer management (Witherspoon, 1986), and hydrocarbon exploitation (Nelson, 2001). Systematically documenting near-surface fracture patterns is essential, for example, in mining applications where they often provide clues to ore deposit patterns (Jelsma et al., 2004), and in geotechnical engineering, where fractures influence stability in human-made structures such as tunnels (Lei et al., 2017).

https://doi.org/10.5194/se-2021-45
Preprint. Discussion started: 21 April 2021

An important property of natural fracture networks (NFRs) is that of *spatial organization* which means that the arrangements are not random but follow a statistically discernable pattern. One can view the spatial arrangement of fractures as a set of objects within a geographical reference system. Within such a framework, fracture objects are either clustered, periodically-spaced, irregularly spaced, or regularly-spaced (Laubach et al., 2018). An alternate framework is a network, where fracture objects are described in relation to one another (Valentini et al., 2007; Andresen et al., 2013; Sanderson and Nixon, 2015). Regardless of how ~~fractures'~~ spatial arrangement is defined, quantitative analysis of spatial arrangements invariably leads to quantification of spatial variation. Fracture networks exhibit considerable spatial variability in their organisation. The physical phenomena commonly used to explain such variation are stress shadowing, layer thickness differences, host rock lithology, layered mechanical anisotropy, high-strain events such as faulting/folding, and diagenesis. It is generally not easy to associate a type of spatial arrangement to any unique set of input boundary conditions as similar loading paths can lead to diverging patterns, and dissimilar loading paths can lead to converging patterns (Laubach et al., 2019).

Quantifying variations in spatial arrangements of fractures involves the sampling of fracture data. Such quantifications can be in the form of 1D (using scanline methods, borehole sampling), in 2D (fracture trace maps from outcrop imagery), or 3D (ground-penetrating radar, microseismic). 1D scanlines provide a method to quantify arrangements and variation, and several statistical measures have been proposed such as fracture spacing (Priest and Hudson, 1976), fracture intensity (Dershowitz and Herda, 1992), coefficient of variation (Gillespie et al., 1993), normalized correlation count (Marrett et al., 2018), and cumulative spacing derivative (Bistacchi et al., 2020). These measurements, however, only indicate the variation of fracture arrangements on the scanline and fail to depict the variation in directions away from the scanline direction. Other issues are associated with scanlines such as censoring and truncation effects, scale-dependence, and minimum sample size requirements.

2D fracture trace maps are especially useful as this type of data combines both geometric and topological information in the form of a network. Recent advances in UAV-photogrammetry (Bemis et al., 2014; Bisdom et al., 2017) and automated image processing algorithms (Prabhakaran et al., 2019) have led to large datasets of 2D fracture traces that reveal much more about network attributes than is possible from 1D sampling. Given such large datasets with rich information, it is pertinent to directly quantify spatial variation from the network structure. Spatial fracture persistence (Dershowitz and Herda, 1992) can quantify 2D spatial variation but only considers some aspects of the network (such as the sum of trace lengths, number of traces, etc., within a sampling region). There is a need for more advanced techniques that are specific to 2D fracture trace data and which can make use of the combined geometric and topological structure.

From a geostatistical perspective, the concept of spatial variability describes how a measurable attribute varies across a spatial domain (Deutsch, 2002). Quantifying magnitude and directional dependence of the variability can also be done using geostatistical tools, provided there is a means to measure variability across multiple spatial samples. The variability in fracture data has typically been reduced to variability in attributes (such as fracture length by sampling area, number of intersections, number of sets, orientations, etc.), and attribute variability used to make decisions of *stationarity*. The identification of representative element volumes (REVs) then follows from the choice of stationarity. However, given that any given spatial network (except regular lattices) is inherently non-stationary, the suitability of such REVs based on stationarity assumptions needs to be

https://doi.org/10.5194/se-2021-45
Preprint. Discussion started: 21 April 2021


Solid Earth Discussions

re-examined. Therefore, it is of interest to compare network variation (rather than attribute variation) across the spatial domain. Any comparative method must retain topological and geometric structures encoded within the spatial samples.

2 Graph theory in fracture network analysis

2.1 Fracture networks as graphs

Many authors have suggested using graph theory for the characterization of fracture networks (Valentini et al., 2007; Andresen et al., 2013; Vevatne et al., 2014; Sanderson and Nixon, 2015; Sanderson et al., 2019). In graph theory and network science, graphs are structures that comprise a set of edges and vertices representing relationships between data. In fracture networks, the vertices are intersections between fractures and the edges represented by fracture segments connecting the vertices. By assigning positional information to the vertices (also nodes), fractures in the form of graphs encapsulate both topological and spatial information. An alternate graph representation is when fractures from tip-to-tip are vertices, and intersections with other fractures are edges. Barthelemy (2018) refers to these types of representations as the *primal* and *dual* forms respectively. Others such as Doolaeghe et al. (2020), call the two representations as *intersection graphs* and *fracture graphs*.

We depict an example of a fracture network in its primal form (see Fig. 1.a) and in its dual form (see Fig. 1.b). The degree of a graph node is simply the number of edges ~~that intersect the~~ particular node. As can be seen in the case of the primal graph in Fig. 1.c, the maximum node degree is 6, with the most common degree value being 3. This type of degree distribution is typical for a spatial graph in which physical constraints limit the maximum possible degree of a node. In the case of the dual graph, as depicted in Fig. 1.d, the maximum degree can be much higher, and the longest fractures that have the highest number of intersections also have the highest degree. Andresen et al. (2013) and Vevatne et al. (2014) suggested that fracture networks are therefore *disassortative* in that shorter fractures preferentially attach on to the longer fractures. Prabhakaran et al. (2021b) also found such a correlation between dual graph node degree and length.

In the graph representation, the weights assigned to edges are proportional to the importance of that edge. In the case of fracture networks in the primal form, this can be the euclidean distance between the nodes (or fracture edge intersections). The weight may also be the direction cosine of the particular edge that indicates orientation. In the dual graph representation, intersections between fractures represent the edges. Therefore the edge weight may be specified in terms of intersection angle.

https://doi.org/10.5194/se-2021-45
Preprint. Discussion started: 21 April 2021

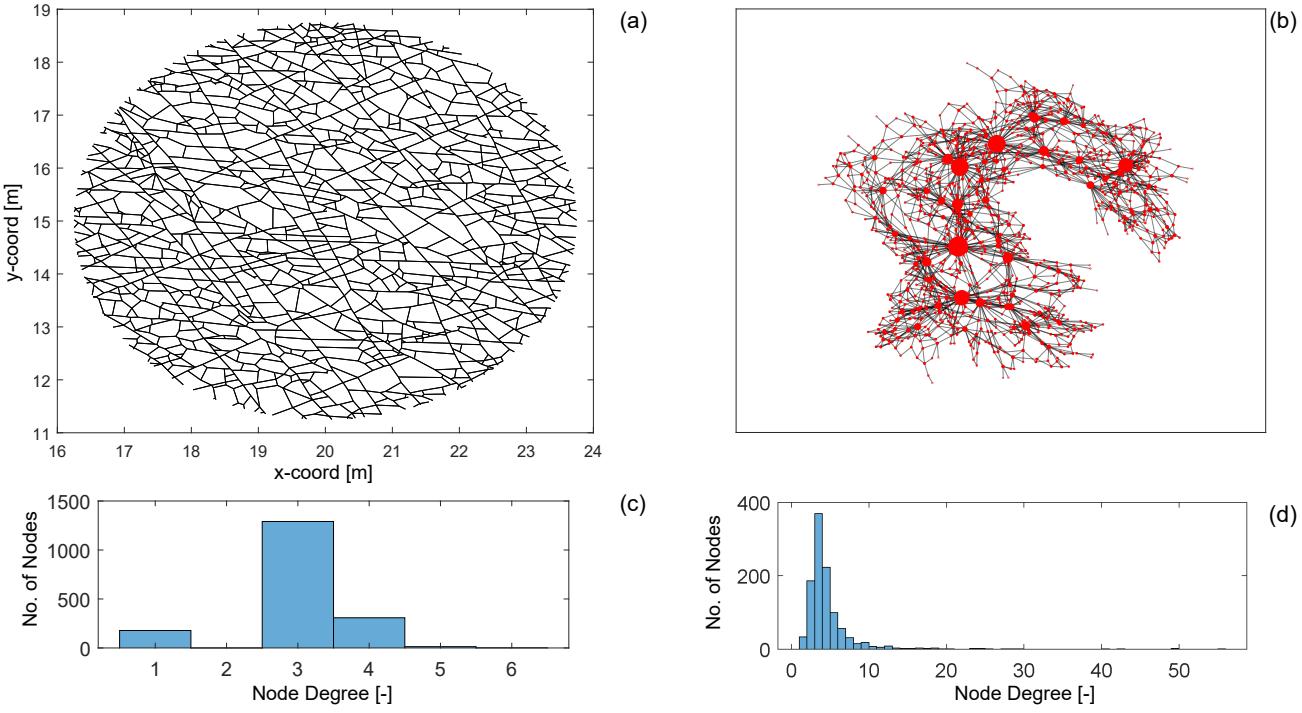

Figure 1. Comparing primal and dual forms of a fracture network from data published by Prabhakaran et al. (2021b) (a) a fracture network depicted in the primal form with dimensions in metres (b) corresponding dual representation of the fracture network with node sizing proportional to dual graph node degree, plotted using a force layout (c) node degree distribution of primal graph (d) node degree distribution of the dual graph

2.2 Graph distance measures to quantify network similarity

Several graph similarity measures exist within the graph theory literature to compare graphs (see Hartle et al., 2020; Tantardini et al., 2019; Emmert-Streib et al., 2016 for recent reviews). Graph comparisons are a challenging, non-trivial problem in terms of computing complexity (Schieber et al., 2017). Still, various measures exist that can capture and highlight useful aspects of the graph structure that facilitate comparisons. Graph *similarity* may be differentiated from graph *isomorphism* in that the latter comparison can only return a binary outcome. An isomorphism test on two graphs G_1 and G_2 can only yield two results, either isomorphic or not. Graph similarity on G_1 and G_2, on the other hand, should return a real-valued quantity that converges to zero when the two graphs approach isomorphism (or complete similarity).

Tantardini et al. (2019) classify distance measures based on whether the metric is capable of comparing graphs with an unequal number of nodes or not. The metrics may also be classified based on whether they can also handle weighted and directed graphs. In the case of spatial graphs derived from fracture networks, an undirected but weighted representation is

https://doi.org/10.5194/se-2021-45
Preprint. Discussion started: 21 April 2021

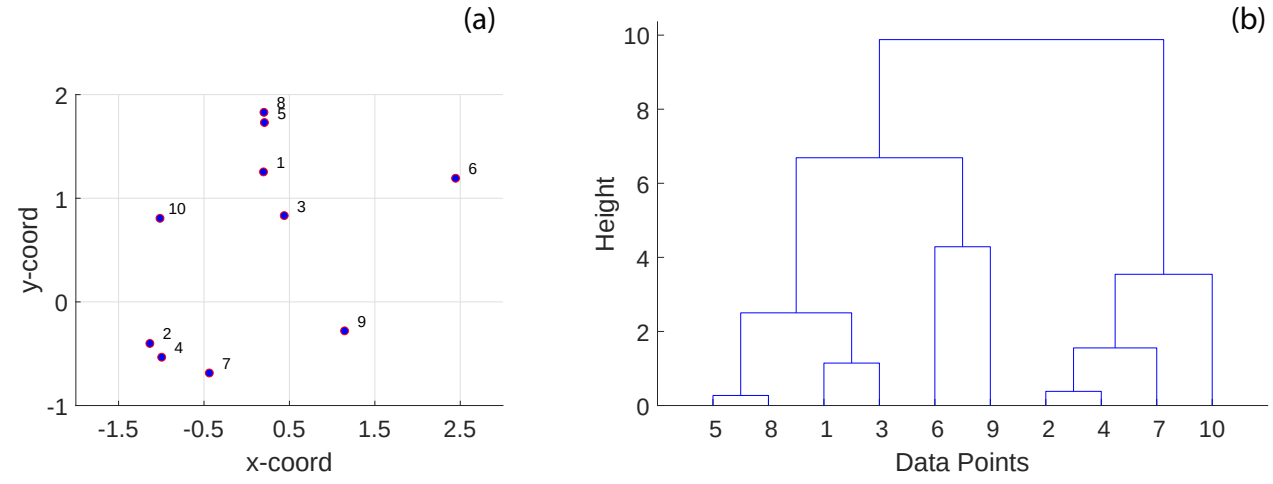

Figure 2. A simple example of hierarchical clustering using euclidean distance (a) 10 randomly positioned points (b) dendrogram computed from hierarchical clustering using the euclidean distance depicting clusters of the 10 individual points at different levels organized into a hierarchy

sufficient. Using a graph-similarity measure on a fracture network, we can explore spatial variations in network structure by comparing multiple sampling points.

2.3 Combining dissimilarity measures with clustering algorithms

Since we are interested in quantifying spatial variability, we may recast the problem as that of identifying clusters within the network. Clustering is also referred to as unsupervised classification and is a process of finding groups within a set of objects with an assigned measurement (Everitt et al., 2011). If we consider a dataset, $D = [X_1, X_2, ...X_n]$, containing 'n' data samples, clustering then implies arranging the elements of D into 'm' distinct subsets, $C = [C_1, C_2, ...C_m]$, where $m \leq n$. From a statistical perspective, the clustering task is different from classification because the former is *exploratory* whereas the latter is *predictive* although both attempt to assign labels. Therefore clustering must precede classification.

In the existing literature on fracture networks, assigning labels to specific perceived archetypal networks (or end-members) is standard. These typologies include terms such as orthogonal, nested, ladder-like, conjugated, polygonal, corridors, etc. (Bruna et al., 2019a,b; Peacock et al., 2018). However, when faced with the reality of outcrop-derived 2D fracture trace data, it is not easy to assign such labels. Therefore, clustering is a significant and necessary step in exploratory fracture data analysis.

~~HC~~ is an unsupervised statistical clustering method (Kaufman, 1990) which can identify clusters within a set of observations given a distance matrix computed by applying a well-defined distance function, pair-wise on each observation. In contrast to other clustering methods such as *k-means* or *k-medoids* which require an a priori known number of clusters as input arguments, HC re-organizes observations into hierarchical representations from which the user can pick a level of granularity. At the lowest level, there is just one cluster containing all the observations. At the highest level, the number of clusters are equal to the

https://doi.org/10.5194/se-2021-45
Preprint. Discussion started: 21 April 2021

observations. HC algorithms are referred to as *agglomerative* or *divisive* depending upon whether they begin from a lower level or from the highest level. The clustering then organises the discrete data into a hierarchical dendrogram structure that positions the clusters based on magnitude of similarity. By combining graph distance computations across spatially distinct samplings with unsupervised HC, cluster detection automatically leads to quantified spatial variation. A simple example of HC on a set of randomly distributed points in space is depicted in Fig. 2 with the associated dendrogram structure.

3 Fracture Datasets

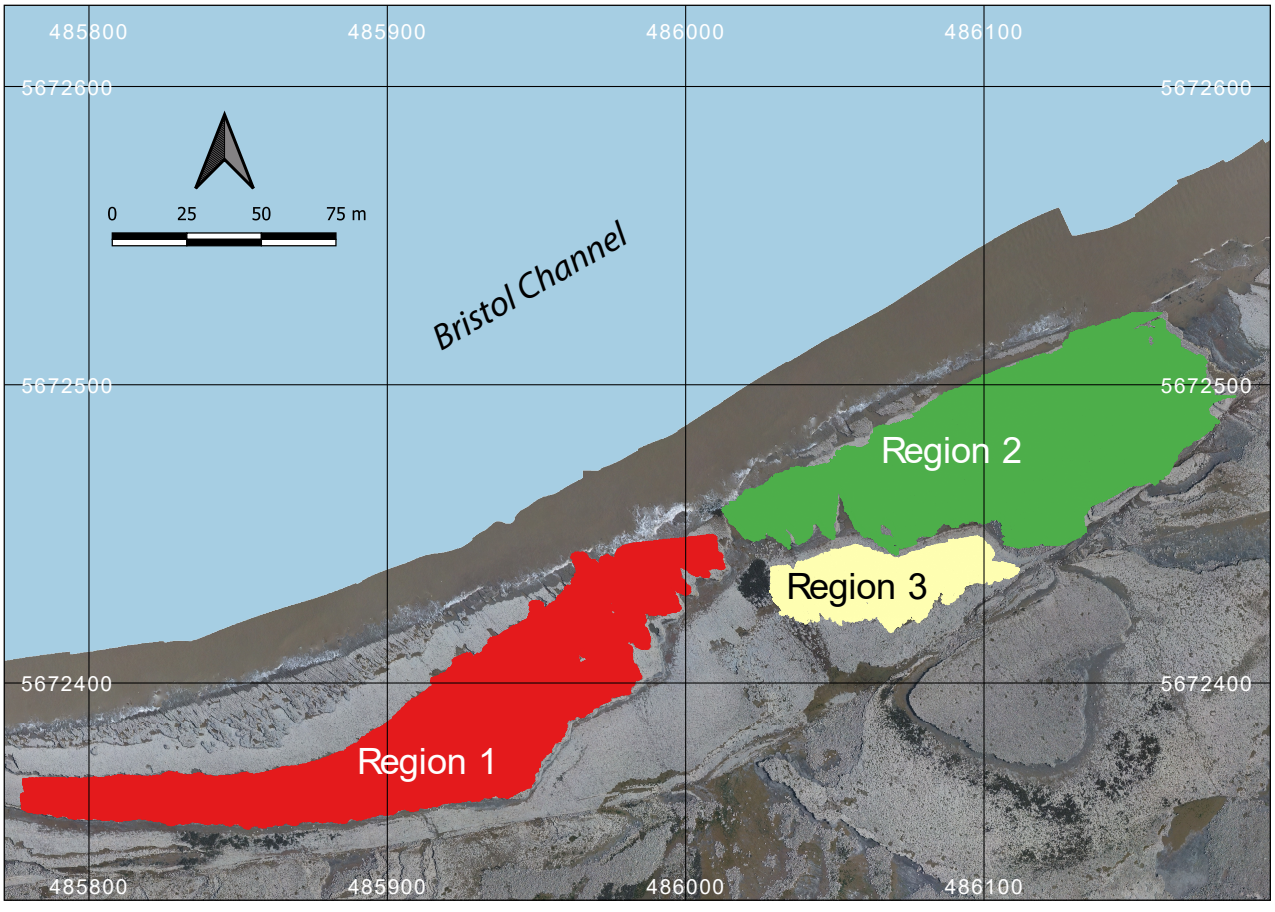

Figure 3. Overview of fracture networks corresponding to the three considered regions. This map is derived from an opem image dataset published by Weismüller et al. (2020) and available for download with a CC-BY license

To validate the proposed approach based on graph distance metrics and hierarchical clustering, we utilize a 2D fracture dataset from the Lilstock pavement in the Bristol Channel, UK (Prabhakaran et al., 2021b). The dataset consists of fractures

https://doi.org/10.5194/se-2021-45
Preprint. Discussion started: 21 April 2021

automatically traced using a technique described in Prabhakaran et al. (2019) from UAV photogrammetric data published by Weismüller et al. (2020). The fracture networks correspond to Jurassic limestones with very dense joint networks spread across multiple layers. The joints are stratabound and perpendicular to bedding. There is considerable spatial variation in the jointing. From previous literature documenting joints within the Lilstock pavements, the spatial variation is attributed to multiple reasons. These include:

- proximity and influence of faults explained by fluid-driven radial-jointing emanating from asperities within fault (Rawnsley et al., 1998; Gillespie et al., 1993 etc)
- spatial variation of thicknesses of intercalated limestone and shale layers (Belayneh, 2004)
- proximity to high-deformation features such as folding (Belayneh and Cosgrove, 2004)
- interplay between regional and local stresses resulting in complex stress fields (Whitaker and Engelder, 2005)
- inheritance from spatial distribution of pre-existing vein / stylolite networks that influenced later joint network development (Wyller, 2019; Dart et al., 1995)

From this dataset, we utilize fracture networks corresponding to three contiguous regions. Figure. 3 depicts the three areas' spatial extent labelled as Regions 1 to 3. The intensity of fracturing is such that the spatial graphs corresponding to each region have a single connected component. Table 1 tabulates summary statistics for the three networks. What is referred to as *fractures* in this Table 1 are sequences of graph edges that are clubbed together based on continuity and a strike direction threshold. Regions 1 and 2 correspond to a single stratigraphic layer but owing to erosion they are not contiguous within the outcrop. We treat them separately in our analysis of spatial variation.

Table 1. Summary statistics for the three regions

Region	Approx. area (sq.m)	Fractures	Edges	Nodes
Region 1	6017	124006	364703	228661
Region 2	6749	141344	365333	235089
Region 3	1473	28892	78151	49771

The networks have significant intra- and inter-network variability in fracturing. Figure. 4 illustrates these differences. The fracture orientations of Region 1 depict discernable angular bins of fracture orientations. On the other hand, rose plots of Regions 2 and 3 show considerable scatter owing to the presence of long and curved fractures. The length distributions are also different, with Region 2 having the longest fractures and Region 1 the shortest. The long fractures in Regions 2 and 3 also exhibit large degrees of curvature, as can be seen when fractures are plotted based on logarithmic length bins. The distribution of joints within a particular length bin is also highly variable.

https://doi.org/10.5194/se-2021-45
Preprint. Discussion started: 21 April 2021

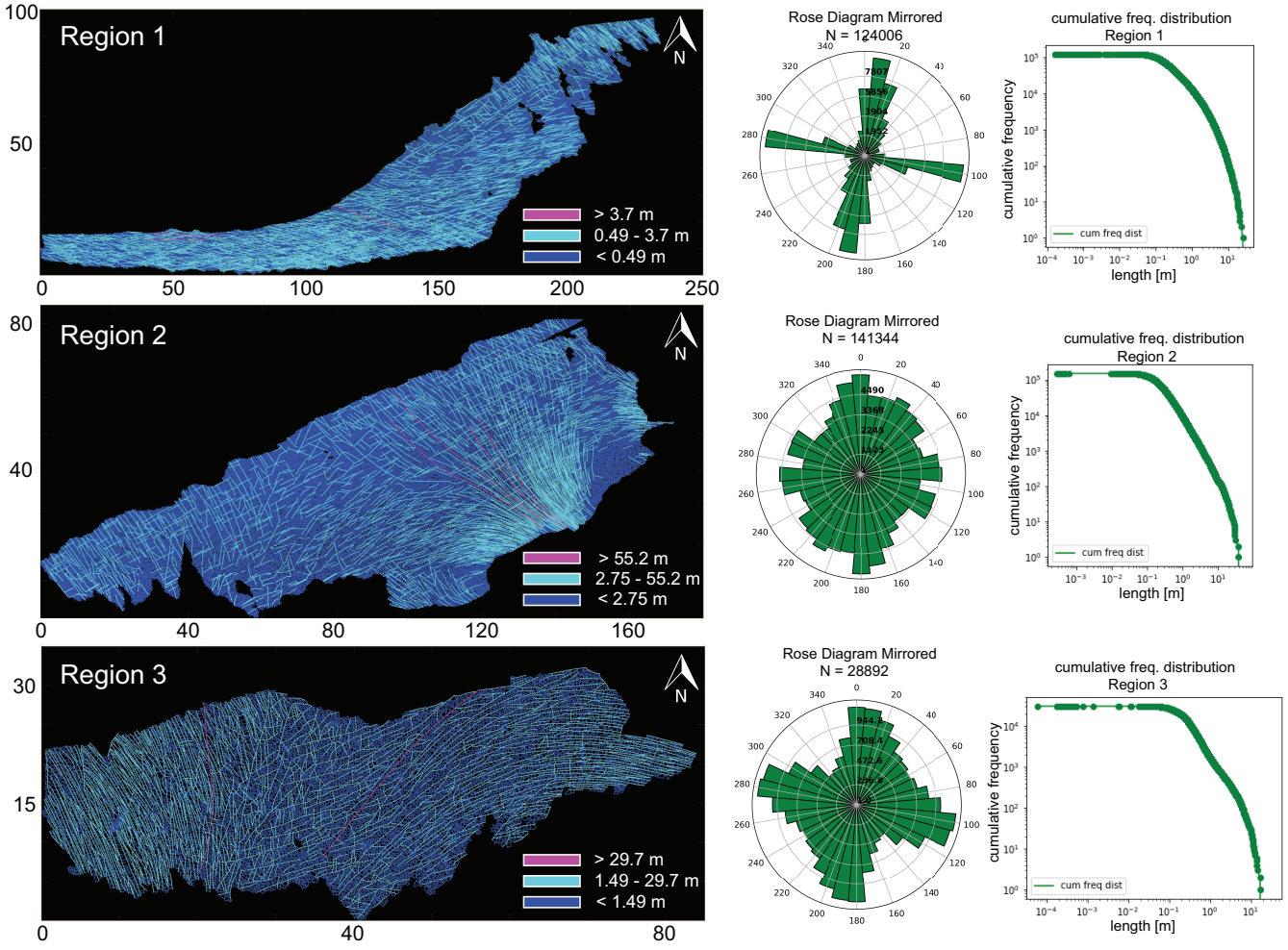

Figure 4. Comparison of the three regions in terms of networks, orientations and length distributions. Map dimensions are in metres. This image has been modified from Prabhakaran et al. (2021b) with permission

4 Methods

4.1 Sub-sampling the network data

We circularly sample the fracture networks on a cartesian grid with a sub-graph extracted within a circular region centered at each grid point. The grid spacing-to-circle diameter is maintained such that neighboring sub-graphs share some portion of the area (see Fig. 5).Near the networks' boundaries, the sub-graphs are either too small or result in disconnected graph components. We neglect these samples so that they do not affect the clustering results. The process of circular sampling creates edge nodes with degree 1 which has the effect of altering node topology by introducing isolated, degree-1 nodes. To prevent this from having an impact on clustering results, we remove all edges from the sub-graphs emanating from degree-1 nodes that contact

https://doi.org/10.5194/se-2021-45
Preprint. Discussion started: 21 April 2021

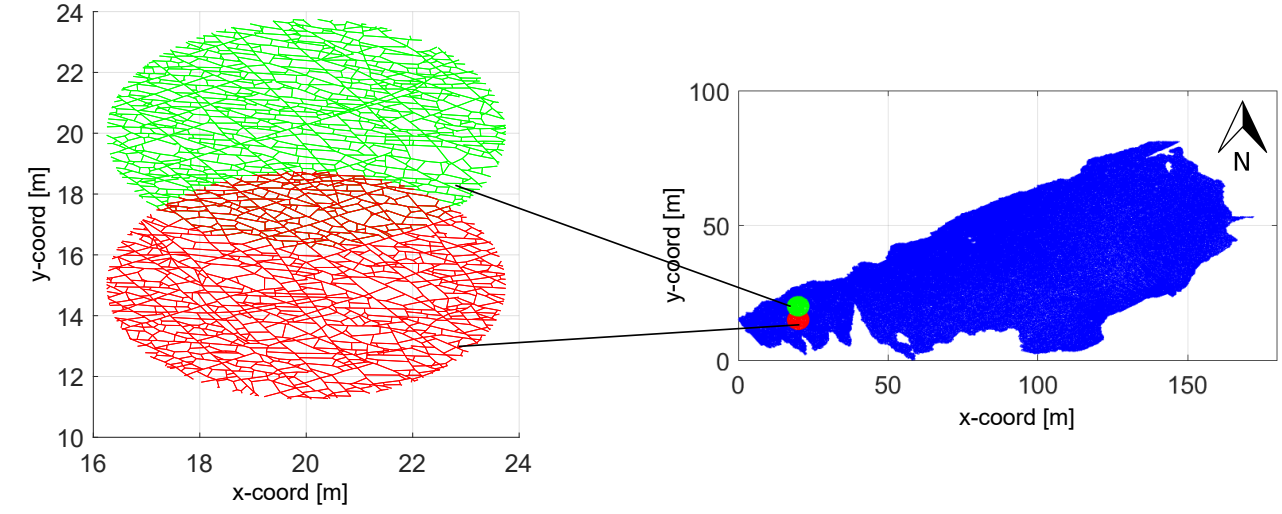

Figure 5. Sub-sampling of a fracture graph corresponding to full region into sub-graphs of 7.5 m diameter and spacing of 5 m

the periphery of the circular sample. This effect is illustrated in Fig. 6. Each sub-graph can now be compared to every other sub-graph using a graph distance metric to compute a pair-wise distance matrix. The distance matrix serves as the input to the hierarchical clustering algorithm.

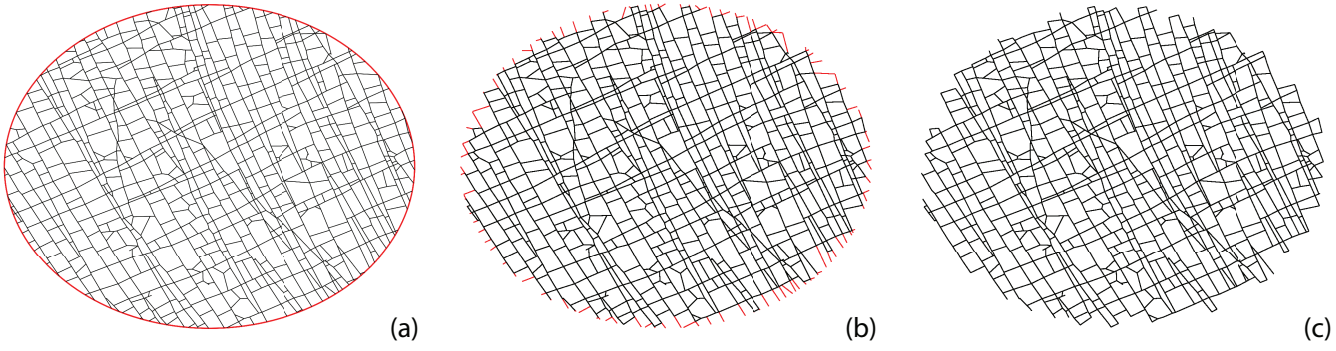

Figure 6. Treating isolated nodes and dangling edges that arise due to circular-sampling (a) circularly ampled subgraph with a diameter of 7.5 m (b) edges connected to isolated nodes intersected by circle (c) subgraph after removing isolated nodes and corresponding dangling edges

For N sub-graphs, the number of comparisons necessary are $\frac{N(N-1)}{2}$. The computational complexity of graph comparison increases polynomially with the size of sub-graphs in terms of node sizes. Since the number of comparisons also increases quadratically with the number of sub-graphs, we seek to balance grid spacing and sampling diameter. For Regions 1 and 2, we choose a spacing of 5 metres for circularly-sampled subgraphs with a diameter of 7.5 m. For Region 3, which is also the

https://doi.org/10.5194/se-2021-45
Preprint. Discussion started: 21 April 2021


Solid Earth Discussions

Table 2. Number of subgraphs obtained per region

Region	No. of sub-graphs
Region 1	219
Region 2	212
Region 3	117

smallest region, a spacing of 5 metres would lead to quite a smaller number of sub-graphs. Therefore, we use a more dense spacing of 3 metres with a diameter of 7.5 m. Table 2 tabulates the number of sub-graphs pertaining to each region.

4.2 Graph similarity measures

We use the following four graph similarity measures to compare the sub-graphs.

- Fingerprint Distance (Louf and Barthelemy, 2014)
- D-measure (Schieber et al., 2017)
- NetLSD (Tsitsulin et al., 2018)
- Portrait Divergence (Bagrow and Bollt, 2019)

The performance of these similarity measures has been validated previously by Hartle et al. (2020) and Tantardini et al. (2019) for a variety of benchmark graph datasets. Each similarity measure is described briefly in the following subsections.

4.2.1 Fingerprint distance

The fingerprint distance introduced by Louf and Barthelemy (2014) is purely geometric and combines statistics of block faces and shape factors in computing a probability distribution of a spatial graph. This measure was formulated in the context of quantifying differences in street patterns. A *block* denotes the 2D region enclosed by graph edges. For any given spatial graph, this corresponds to the number of bounded sub-graphs or primary cycles. Isolated fractures and those having dead ends are neglected when computing these blocks. Given the network intensity in our dataset, such isolated fractures are minimal. Every block has an associated *shape factor*, 'ϕ' which is expressed in terms of block area 'A' and circumscribing circle area, 'A_c' ,

$$\phi = \frac{A}{A_c} \tag{1}$$

The value of ϕ is always smaller than 1, with larger values meaning greater regularity. No unique correspondence exists between a particular shape and a magnitude of ϕ; however, the overall distribution of ϕ indicates regularity within a network and highlights differences between spatial graphs. Shape factor alone does not fully serve as a similarity measure as blocks can have similar shapes but different face areas. The distribution of the block-face regions is binned logarithmically to integrate

https://doi.org/10.5194/se-2021-45
Preprint. Discussion started: 21 April 2021

information from the shape factor and block area distributions. A conditional probability distribution, $P(\phi|A)P(A)$, is then defined representing the contribution of $P(\phi)$ for each area bin and the summation of which yields the fingerprint curve, $P(\phi)$,

$$P(\phi) = \sum_{A} P(\phi|A)P(A). \tag{2}$$

An example of a *fingerprint*, so named by Louf and Barthelemy (2014), is depicted in Fig. 7 with the distribution curves for three area bins. The curve encapsulates information based on shape factors and block areas, including the proportional contribution from all logarithmic area bins considered. Denoting $f_\alpha(\phi)$ as the ratio of the number of faces with a shape factor 'ϕ' that lie in a bin 'α' over the total number of faces for that graph, a distance d_α between two graphs G_a and G_b is computed by integrating over $f_\alpha(\phi)$ for the two different graphs. The distance based on $f_\alpha(\phi)$ of the two graphs for a single area bin is defined as:

$$d_\alpha(G_a, G_b) = \int_0^1 |f_\alpha^a(\phi) - f_\alpha^b(\phi)|^n d\phi \tag{3}$$

As per Louf and Barthelemy (2014), the value of n can either be 1 or 2. We choose $n = 1$ in our computation. The global fingerprint distance D_{FP} between G_a and G_b can then be computed summing over all area bins α,

$$D_{FP}(G_a, G_b) = \sum_{\alpha} d_\alpha(G_a, G_b)^2 \tag{4}$$

We have attached our MATLAB implementation of the fingerprint distance in Prabhakaran (2021). We computed the distance matrix for all sub-graphs corresponding to the three regions using this implementation.

https://doi.org/10.5194/se-2021-45
Preprint. Discussion started: 21 April 2021

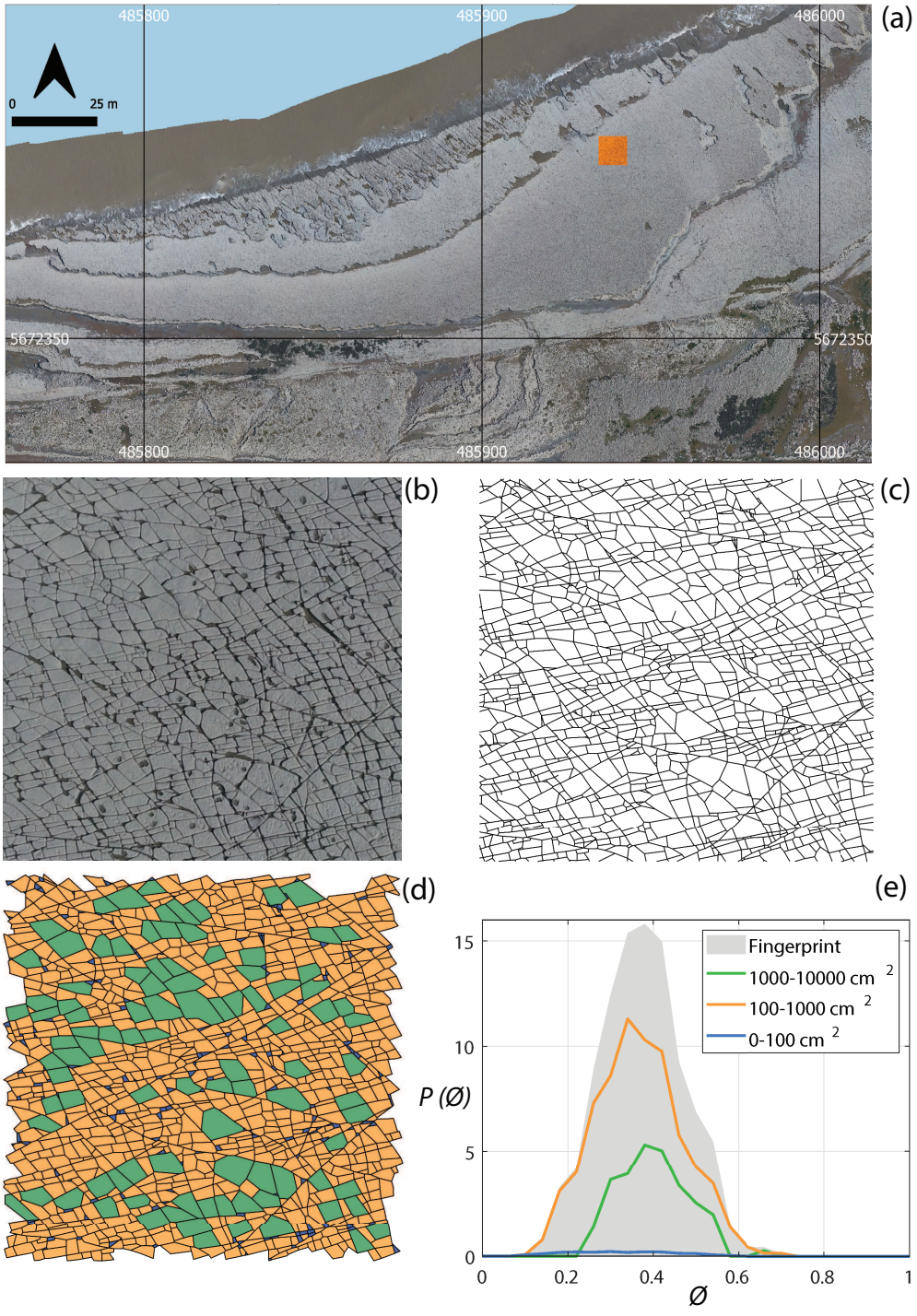

Figure 7. (a) 8.6 m x 6.75 m sub-graph tile from Region 1 highlighted in orange (b) enlarged view of selected image tile (c) fracture network corresponding to image as a spatial graph (d) block face areas coloured as per three area bins, 0-100 cm^2, 100-1000 cm^2, and 1000-10000 cm^2 (e) $P(\Phi)$ or fingerprint of the sub-graph depicting the combined effects of area and shape factor (Φ) pertaining to the three area bins. This map has been created from images contained in the open dataset (CC-BY license) published by Weismüller et al. (2020)

https://doi.org/10.5194/se-2021-45
Preprint. Discussion started: 21 April 2021


Solid Earth Discussions

4.2.2 D-measure

The D-measure introduced by Schieber et al. (2017) is a three-component distance metric with weighting constants for each component. The three properties of graphs compared are the network node dispersion (NND), node distance distribution (μ), and the alpha centrality (α). The dissimilarity measure, D_{DM} is the weighted sum:

$$D_{DM}(g,h) = w_1\sqrt{\frac{\mathcal{J}(\mu_g,\mu_h)}{log2}} + w_2\left|\sqrt{NND(g)} - \sqrt{NND(h)}\right| + \frac{w_3}{2}\left(\sqrt{\frac{\mathcal{J}(P_\alpha(g),P_\alpha(h))}{log2}} + \sqrt{\frac{\mathcal{J}(P_\alpha(g^c),P_\alpha(h^{c'}))}{log2}}\right), \tag{5}$$

where $\mathcal{J}$ indicates the Jensen-Shannon divergence. The constants w_1, w_2, and w_3 in Eq.5 are real and non-negative weights such that $w_1 + w_3 + w_3 = 1$.

As per Schieber et al. (2017) the first term in Eq.5 compares averaged connectivity node's patterns as per node distance distribution. Schieber et al. (2017) defines NND, within the second term, as a measure of the heterogeneity of a graph w.r.t connectivity distances that capture global topological differences. The NND is computed as:

$$NND(G) = \frac{\mathcal{J}(P_1,....,P_N)}{log(d+1)}, \tag{6}$$

where the numerator in Eq.6 is the Jensen Shannon divergence of N connectivity distance distributions $[P_1, P_2.....P_N]$. P_i is constructed as $P_i = p_i(j)$ where $p_i(j)$ is the fraction of nodes connected to node i at distance j. The Jensen-Shannon divergence of $[P_1, P_2.....P_N]$ is expressed as:

$$\mathcal{J}(P_1,....,P_N) = \frac{1}{N}\sum_{i,j} p_i \log\left(\frac{p_i(j)}{\mu_j}\right). \tag{7}$$

μ_j in Eq.7 is the average of N distributions and can be written as,

$$\mu_j = \frac{1}{N}\sum_{i=1}^{N} p_i(j). \tag{8}$$

The third term in Eq.5 is based on probability density functions associated with alpha centrality of graph $P_\alpha(g)$ and alpha centrality of the graph complement $P_\alpha(g^c)$. The value of weights was suggested by Schieber et al. (2017) as $w_1 = w_2 = 0.45$ and $w_3 = 0.1$. We use the implementation provided by Schieber et al. (2017) with these sets of weights to build the distance matrices for all sub-graphs within the three regions of interest.

4.2.3 Portrait Divergence

The Portrait Divergence similarity score derives from *network portraits* introduced by Bagrow et al. (2008) for unweighted graphs and extended to weighted graphs by Bagrow and Bollt (2019). For a graph g with N nodes, the network portrait is

https://doi.org/10.5194/se-2021-45
Preprint. Discussion started: 21 April 2021

defined as a matrix B_{lk} where each entry is the number of nodes with k nodes at l distance. The limits of l and k are $0 \leq l \leq d$ and $0 \leq k \leq N-1$ with d being the diameter of the graph. The row entries of the network matrix B_{lk} are probability distributions of a random node having k nodes at a distance l:

$$P(k|l) = \frac{B_{lk}}{N} \tag{9}$$

For a second graph h, if the network matrix is B'_{lk} with a corresponding probability distribution of $Q(k|l)$ and diameter d', the Kullback Leibler (KL) divergence between $P(k|l)$ and $Q(k|l)$ is expressed as:

$$KL(P(k|l)||P(k|l)) = \sum_{l=0}^{max(d,d')} \sum_{k=0}^{N} P(k,l) log \frac{P(k,l)}{Q(k,l)} \tag{10}$$

The portrait divergence $D_{PD}(g,h)$ is computed by the Jensen Shannon divergence between $P(k|l)$ and $Q(k|l)$:

$$D_{PD}(g,h) = JSD(P(k|l), Q(k|l). \tag{11}$$

This can be expressed in terms of Kullback Leibler divergences and mixture distributions as:

$$D_{PD}(g,h) = \frac{1}{2}(KL(P||M) + KL(Q||M)) \tag{12}$$

where the mixture distribution M of $P(k|l)$ and $Q(k|l)$ is given by:

$$M = \frac{1}{2}(P(k|l) + Q(k|l)) \tag{13}$$

The portrait divergence measure provides a single value $0 \leq D_{PD}(g,h) \leq 1$ for any pair of graphs. Bagrow and Bollt (2019) applied the portrait divergence measure to both synthetic and real world networks. The code implementation of portrait divergence attached with Bagrow and Bollt (2019) is used to construct the distance matrices for all sub-graphs within the three regions of interest.

4.2.4 Laplacian Spectral Descriptor

The NetLSD distance was introduced by Tsitsulin et al. (2018). It is based on a Frobenius norm computed between heat trace signatures of normalized Laplacian matrices of two graphs. For a graph g with a normalized Laplacians L and n nodes, a heat kernel matrix is defined as:

$$H_t = e^{-tL} = \sum_{j=1}^{n} e^{-t\lambda_j} \phi_j \phi_j^T \tag{14}$$

Using the heat kernel matrix H_t, a heat trace h_t is defined as:

$$h_t = \sum_{j=1}^{n} e^{-t\lambda_j} \tag{15}$$

https://doi.org/10.5194/se-2021-45
Preprint. Discussion started: 21 April 2021

For a second graph g' with a heat trace signature of h'_t, the NetLSD distance D_{LSD} is then the Frobenius norm of the two heat signatures as:

$$D_{LSD} = ||h_t, h'_t||_{Frobenius} \tag{16}$$

We use the NetLSD python package implemented by Tsitsulin et al. (2018) to calculate the distance matrices associated with sub-graphs from each region.

4.3 Hierarchical Clustering

After sub-sampling the fracture networks (see Section 4.1) and using the graph distance metrics described in Section 4.2 to construct distance matrices, we apply hierarchical clustering. HC can be done in an agglomerative versus divisive manner (Hennig et al., 2016). We utilize the agglomerative approach, which generally follows the steps described in Algorithm 1. Based on how linking of clusters is done as per Algorithm 1(iii), HC can be classified into methods such as single linkage, complete linkage, unweighted pair-group average, weighted pair-group average, unweighted pair-group centroid, weighted pair group centroid, and Ward's method (Wierzchoń and Kłopotek, 2018). Ward's method performs the linkage by minimizing the sum-of-squares of distances between objects and cluster centre. We use Ward's method implemented within the R statistical programming environment to do the HC for all the sub-graph distance data.

Algorithm 1 Agglomerative Clustering

Input: Data $D = [X_1, X_2, ...X_n]$

Output: Dendrogram $C = [C_1, C_2...C_m]$

(i). *Initialization*. m clusters of one element each with pair-wise distances computed and stored in symmetric square distance matrix D_{dist}

(ii). form pair C_i and C_j that are closest within C

(iii). form cluster $C_k = C_i \cup C_j$ and generate a new dendrogram node

(iv). update D_{dist} after computing distance between C_k and $C - C_k$

(v). delete rows and columns corresponding to C_i, C_j from D_{dist} and add rows and columns pertaining to C_k

(vi). repeat (i) - (v) till only a single cluster remains

5 Results

We visualize HC clusters using heatmaps of distance matrices, dendrograms, and spatial plots. We plot a heatmap of the pair-wise sample distances symmetrically with the associated hierarchy on a dendrogram. This plot along with weighted-sum-of-squares plots enables picking of number of clusters and decisions on the height at which to *cut* the dendrogram. In this section, we present the clustering results in the form of heatmaps, dendrograms, and spatial clusters for all the regions.

https://doi.org/10.5194/se-2021-45
Preprint. Discussion started: 21 April 2021

5.1 Region 1

Table 3 tabulates the cluster results for all four distance measures. Figure. 8 depicts the combined heatmap and dendrogram plots with the identification of five top clusters for each of the four considered distance measures. We choose to depict the top five clusters in the spatial plots to compare results generated for the four distance measures. The spatial distribution of these clusters is overlain over the network in Fig. 9 to compare clustering results for all four distance measures along with spatial fracture persistence P_{20} and P_{21} computed using box-counting (box size of 0.5 × 0.5 m).

Table 3. Summary of sub-graphs within each cluster of Region 1

Metric →	FP	DM	LSD	PD
Cluster 1	83	74	91	85
Cluster 2	71	59	61	44
Cluster 3	36	49	44	33
Cluster 4	26	20	12	33
Cluster 5	3	17	11	24
Total			219	

Clusters in the spatial plot in Fig. 9 are depicted as discs representing each sub-graph with a single colour assigned for every subsample within the cluster. The results indicate different types of cluster partitions for each distance measure. These differences are not immediately observable from the fracture persistence plots in Fig. 9(e) and Fig. 9(f). The clustering resulting from the fingerprint, D-measure, and portrait divergence, immediately show spatial autocorrelation trends as seen in Fig. 9(a), Fig. 9(b), and Fig. 9(d), respectively. NetLSD is the exception depicting a speckled pattern with no discernable smooth variation as is observable in Fig. 9(c).

Figure. 10 depicts the spatial clustering results from the fingerprint distance with cut-out archetypal examples depicting the variation in fracturing. The clustering seems to have a N-S variation trend as observed from the spatial plot. The trend is corroborated by observing the dendrogram which splits into two main branches. The branch corresponding to the southern clusters, depicted in orange and red, further branches out with 83 and 26 subgraph samples. The other branch with sub-branches of 71 and 26 samples, depicted in yellow and light blue correspond to the northern region. An outlier branch exists with 3 samples (in dark blue). The samples extracted from each cluster depicts different styles of fracturing.

A similar variation is observable from the zoomed-in sections of cluster maps for the D-measure distance (see Fig. 11). However, the cluster demarcations are less stark than with the fingerprint distance with a notable stippled pattern. Observing the dendrogram, the region can be divided into a branch consisting of a thin sliver in the N-E (in dark blue) and the remaining area. This branch also includes a sub-branch in orange, which consists of boundary sub-graphs which were partially sampled. These seem to affect the D-measure clustering resulting in the appearance of this boundary cluster. The second branch diverges into a cluster in the western region (in red). The remainder of the region consists of the clusters depicted in yellow that is concentrated in the centre of the region and the light-blue cluster that is the predominant type.

https://doi.org/10.5194/se-2021-45
Preprint. Discussion started: 21 April 2021

The results of PD measure also depict the N-S variation (see Fig. 12) in the clustering. Similar to the D-measure, the PD also seems to be sensitive to subgraph completeness as can be seen by a boundary cluster in orange. Observing further branches of the dendrogram, we can observe a cluster in red which closely correspond to the trend of high fracture persistence (compare with Fig. 9(e) and Fig. 9(f)). Delving deeper into the dendrogram is a cluster (in yellow) corresponding to a thin sliver in the N-E of the region. The remainder of the region consists of a cluster, depicted in blue to the south, and a cluster (in light blue) to the east.

https://doi.org/10.5194/se-2021-45
Preprint. Discussion started: 21 April 2021

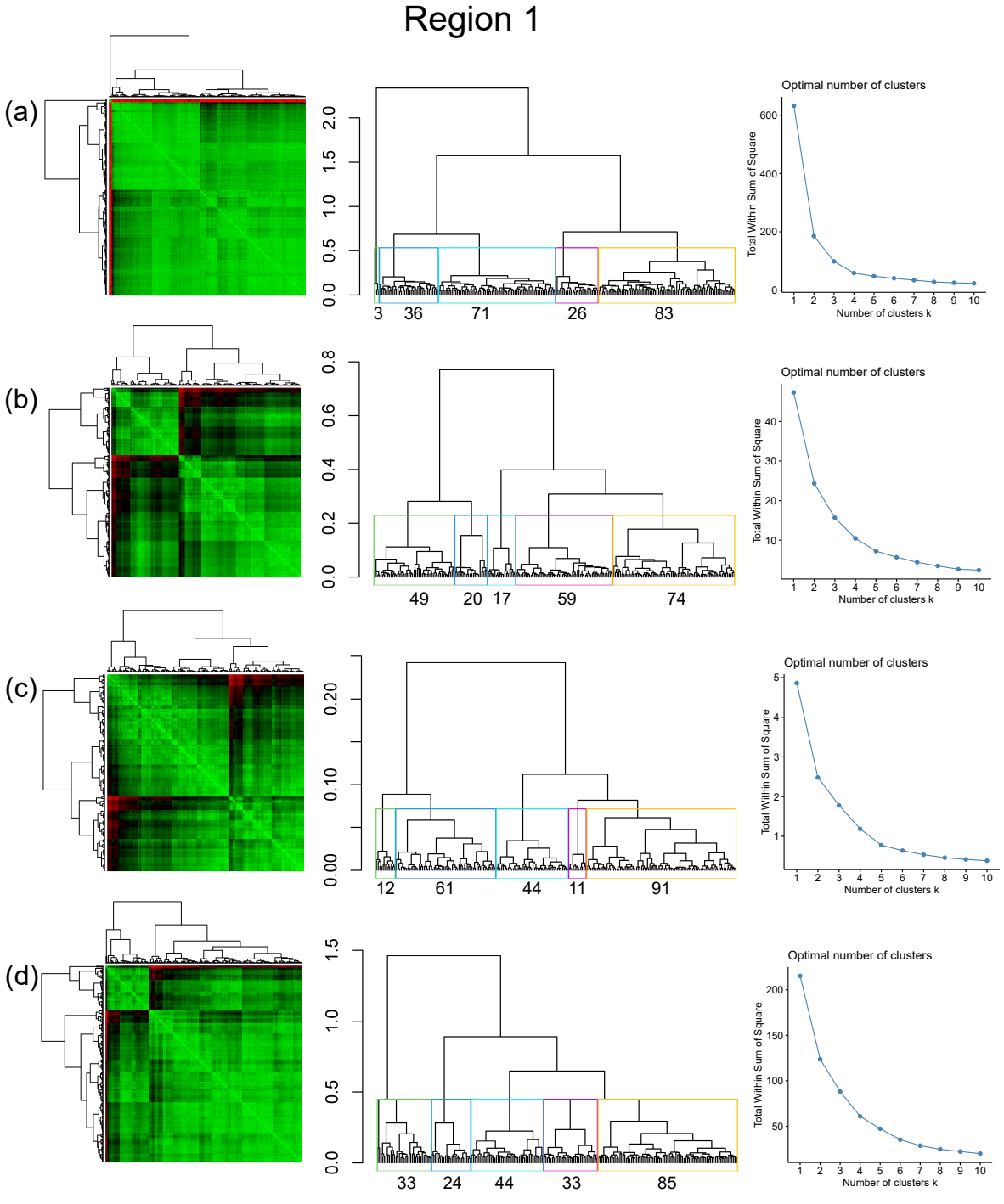

Figure 8. Combined symmetric heatmap of distance matrix and dendrograms, dendrograms with major clusters and sum-of-squares elbow plots for Region 1 (a) Fingerprint (b) D-measure (c) NetLSD (d) Portrait Divergence

https://doi.org/10.5194/se-2021-45
Preprint. Discussion started: 21 April 2021

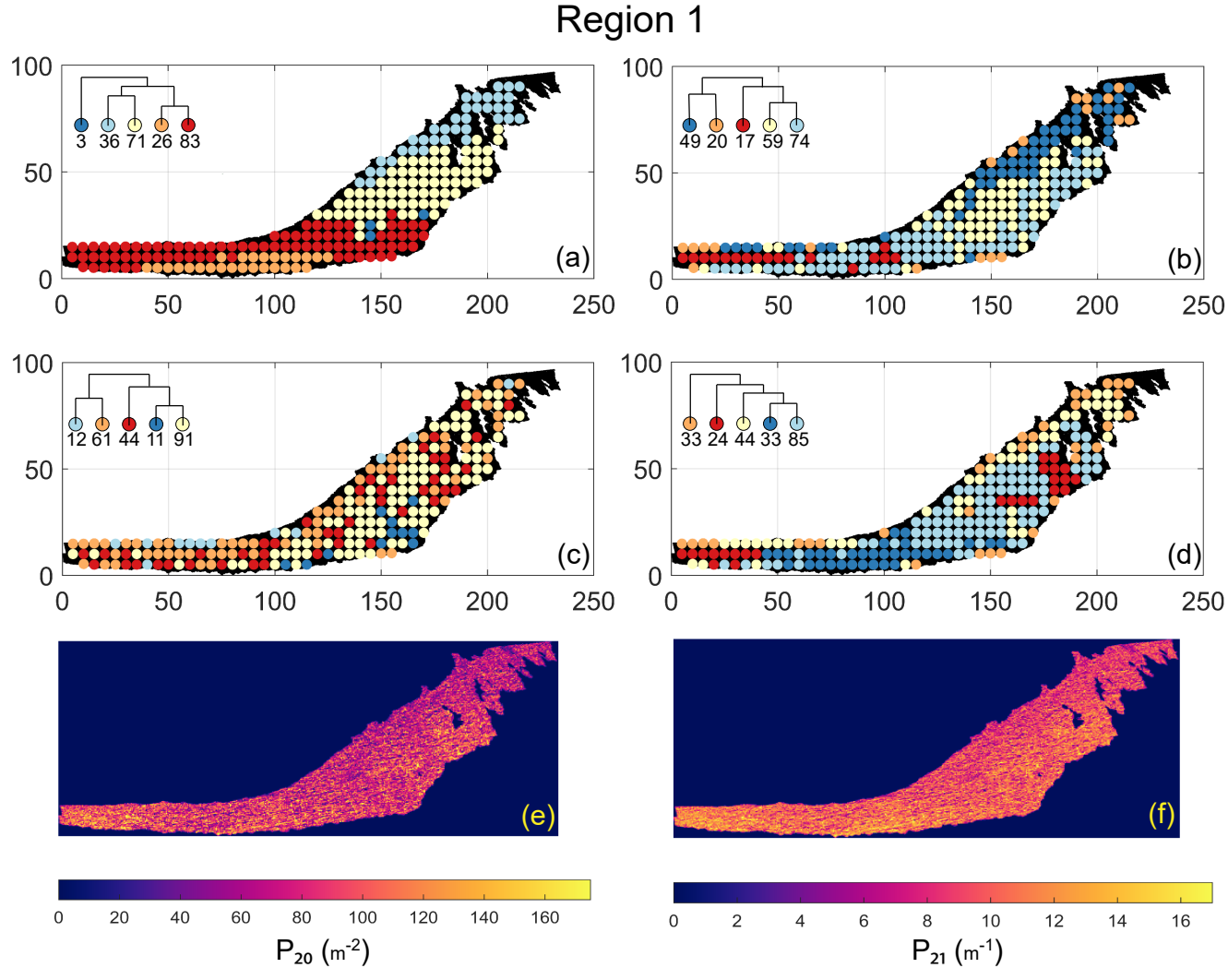

Figure 9. Region 1 clustering results computed using (a) fingerprint distance (b) D-measure distance (c) NetLSD distance (d) Portrait Divergence distance (e) spatial P_{20} (f) spatial P_{21}

https://doi.org/10.5194/se-2021-45
Preprint. Discussion started: 21 April 2021

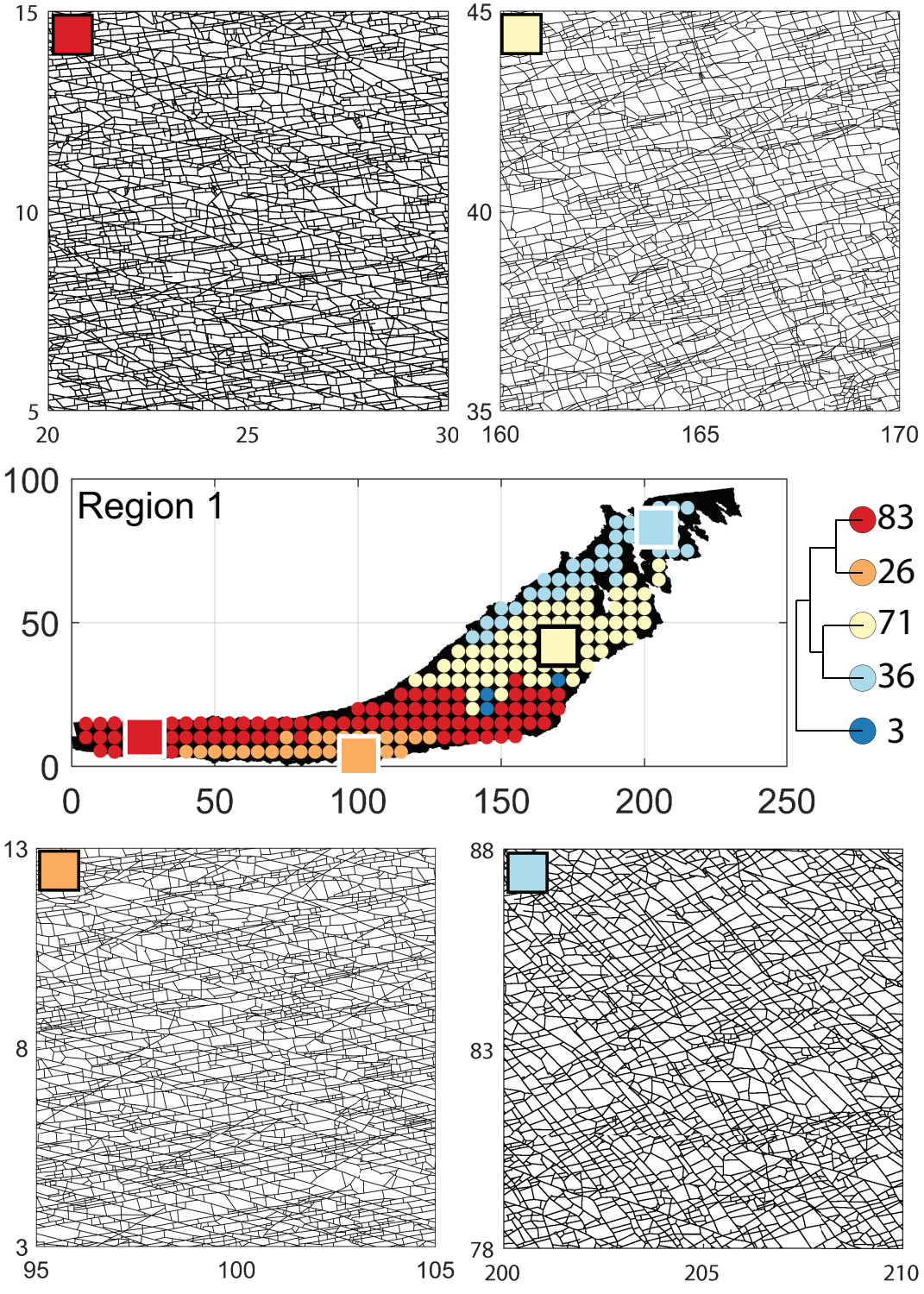

Figure 10. 10 m x 10 m samples depicting variation in fracturing style as identified in the largest four clusters by the fingerprint distance in Region 1

https://doi.org/10.5194/se-2021-45
Preprint. Discussion started: 21 April 2021

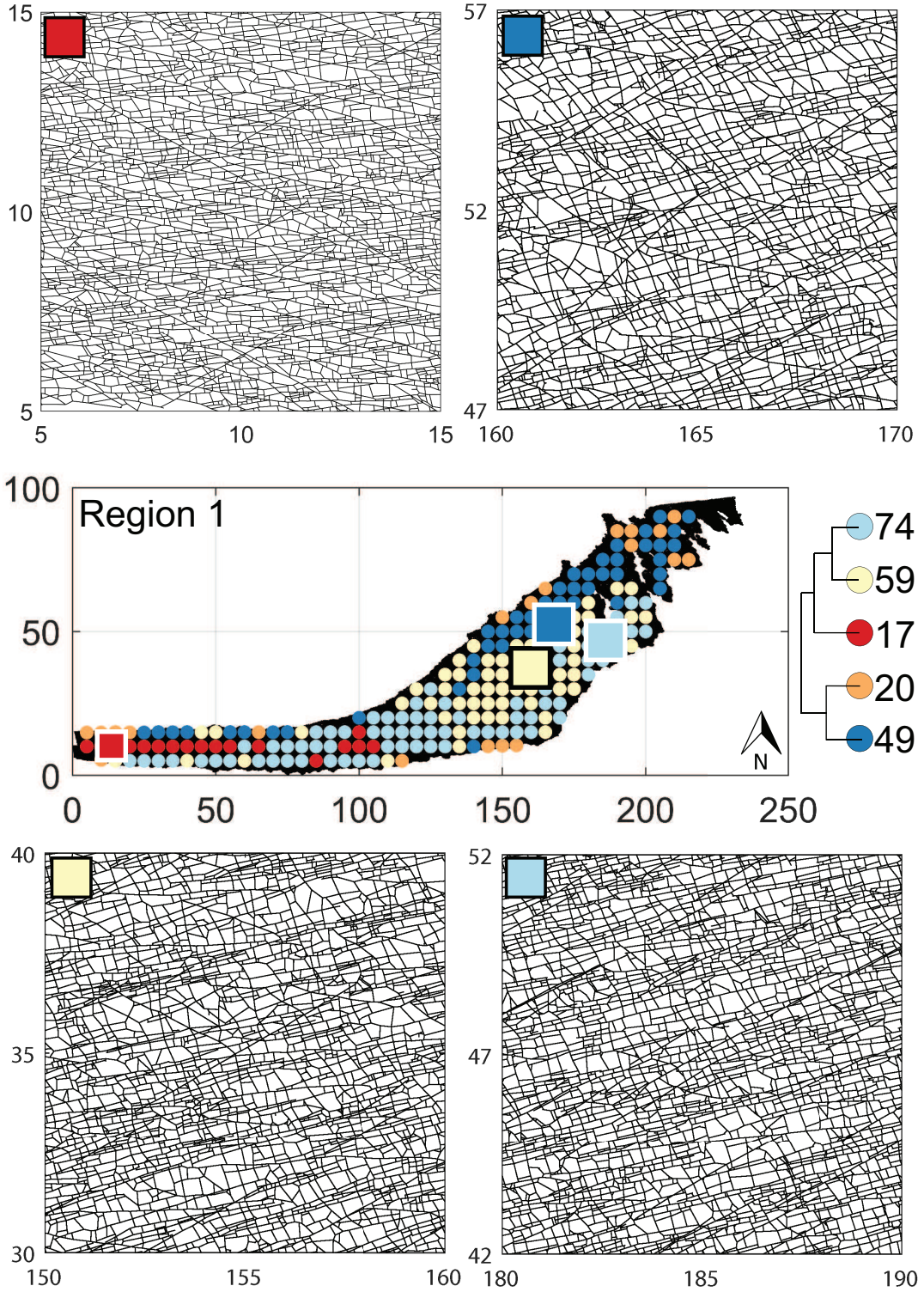

Figure 11. 10 m x 10 m samples depicting variation in fracturing style as identified in the largest four clusters by the D-measure distance in Region 1

https://doi.org/10.5194/se-2021-45
Preprint. Discussion started: 21 April 2021

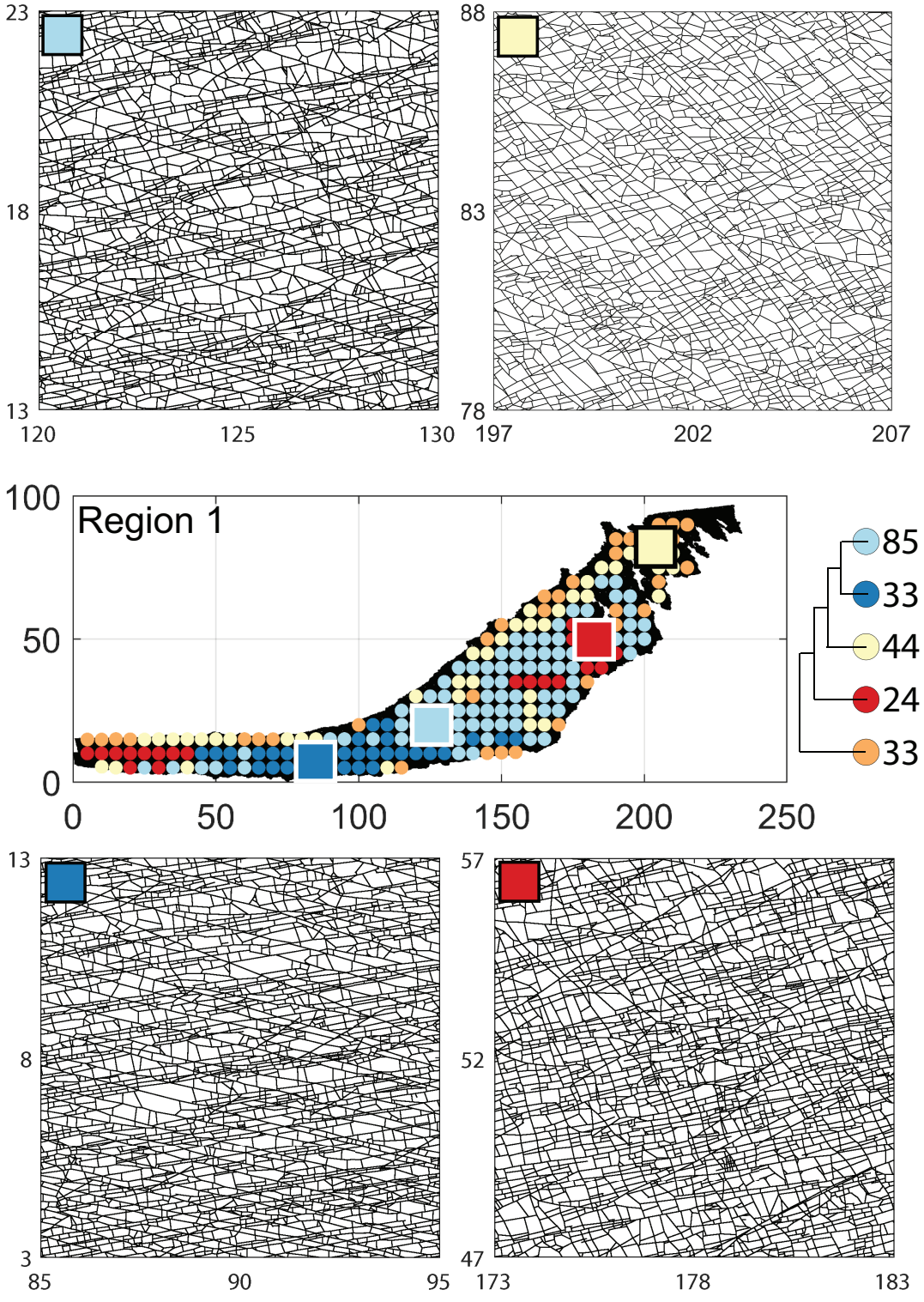

Figure 12. 10 m x 10 m samples depicting variation in fracturing style as identified in the largest four clusters by the portrait divergence distance in Region 1

https://doi.org/10.5194/se-2021-45
Preprint. Discussion started: 21 April 2021

5.2 Region 2

Figure. 13 depicts the combined heatmap and dendrogram result for Region 2. Table 4 tabulates the cluster results. Similar to Region 1, the clusters identified from the four metrics show differences (see Fig. 14), but in Region 2 we are now able to see even more pronounced variation. The FP, DM, and PD show well-demarcated clusters, with LSD showing a speckled clustering. All four measures correctly identify the region of radial fracturing as described by Gillespie et al. (1993). There are clear transition regions away from the influence of the fault located towards the SE of Region2, roughly following fracture persistence trend that progressively increases from SE to NW.

Table 4. Summary of sub-graphs within each cluster of Region 2

Metric →	FP	DM	LSD	PD
Cluster 1	93	49	81	96
Cluster 2	62	47	68	60
Cluster 3	42	39	31	35
Cluster 4	11	39	24	19
Cluster 5	4	38	8	2
Total			212	

The clustering is depicted in further detail for the fingerprint distance in Fig. 15 with 10 x 10 m samples extracted from the major groupings. The smallest cluster (depicted in blue) shows the radial fracturing pattern which changes away from the fault towards the NW as can be seen in the sample labelled in yellow. Further moving NW, the fracturing motif changes again with a noticeable increase in fracture density evidenced by cluster in orange. The westernmost cluster has a different style which may be linked to the north eastern cluster in Region 1.

As is observable from Fig. 16 and similar to the fingerprint, the D-measure also identifies a cluster representing the radial fractures (dark blue). The adjoining cluster away from the fault-affected region depicts a sub-region where the presence of the radial faults has subsided. The fracturing motif is observably more dense towards the NW as evidenced from the cluster in orange. The western-most extremity of Region 2 depicts a visibly different fracturing style (in red).

The clustering identified by the portrait divergence (see Fig. 17) is roughly similar to that of the D-measure. The PD is able to demarcate a smaller region within the radial fractures which correspond to the areas with lowest fracturing density. Also the results seem to be affected by boundary sub-graphs for which the clustering does not show autocorrelation. This is perhaps due to the sub-graphs being incomplete. The PD is also not able to delineate the westernmost cluster which the fingerprint and D-Measure could identify.

https://doi.org/10.5194/se-2021-45
Preprint. Discussion started: 21 April 2021

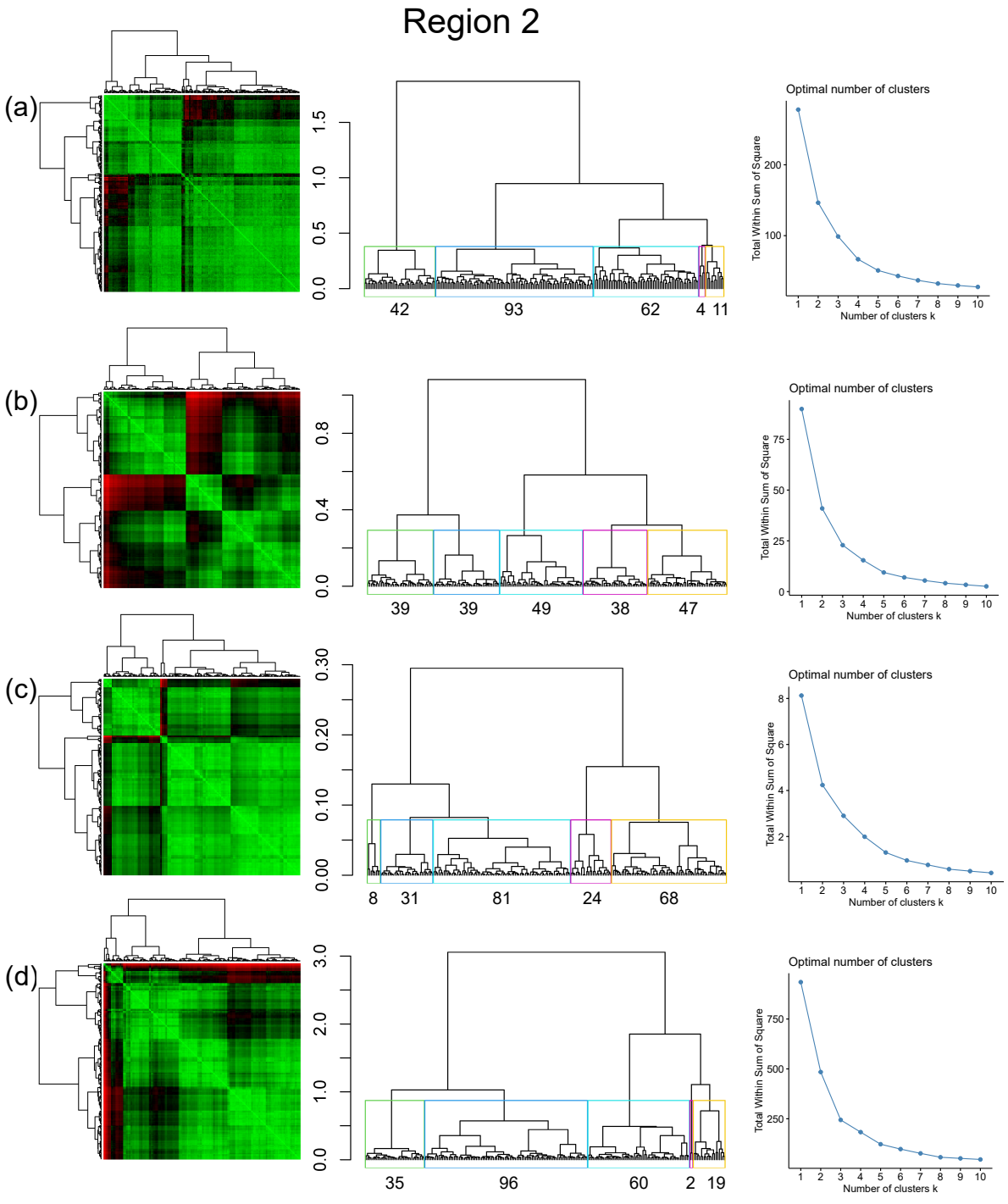

Figure 13. (Combined symmetric heatmap of distance matrix and dendrograms, dendrograms with major clusters, and sum-of-squares elbow plots for Region 2 (a) Fingerprint (b) D-measure (c) NetLSD (d) Portrait Divergence

https://doi.org/10.5194/se-2021-45
Preprint. Discussion started: 21 April 2021

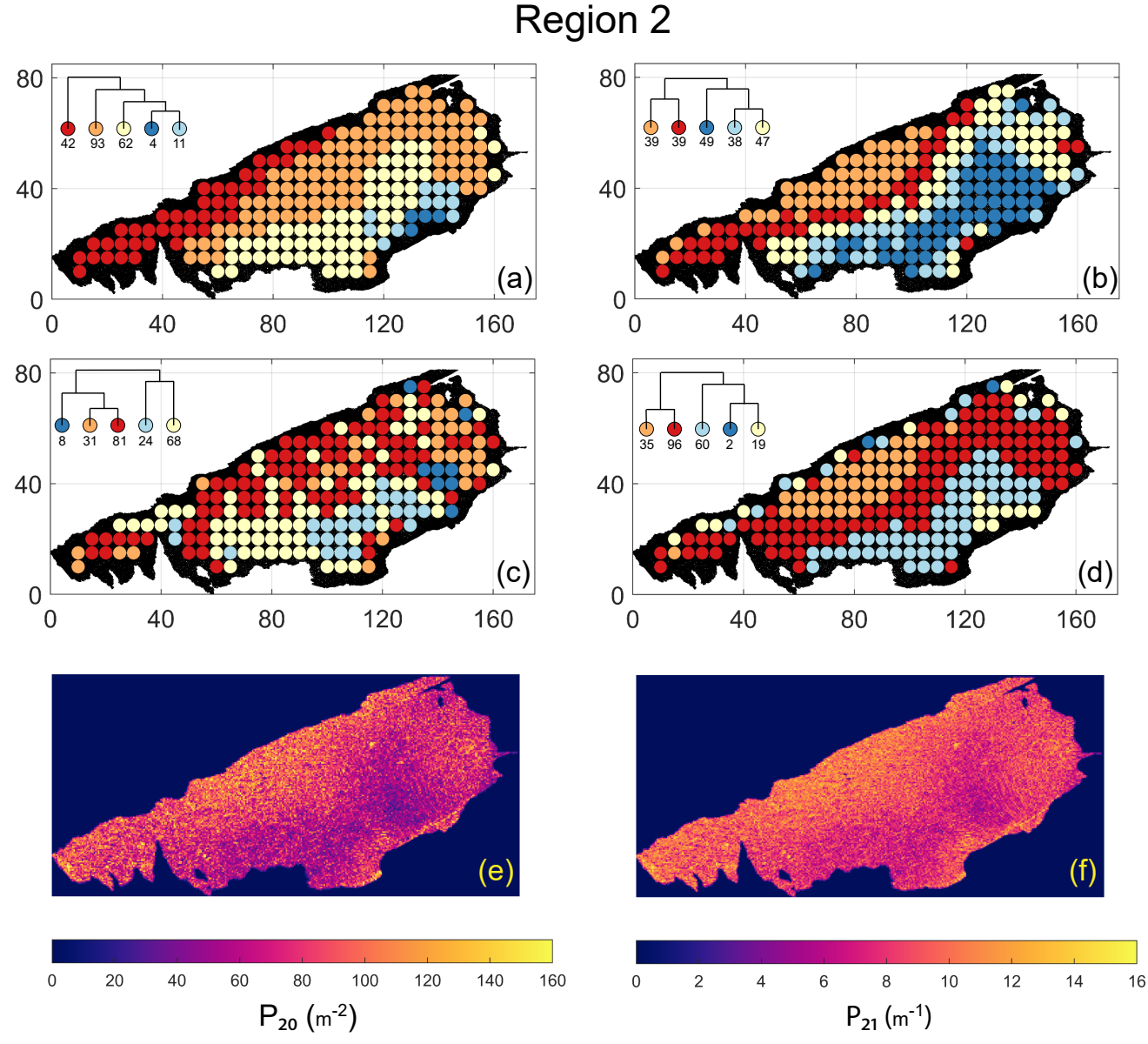

Figure 14. Region 2 hierarchical clustering results computed using (a) Fingerprint distance (b) D-measure distance (c) NetLSD distance (d) Portrait Divergence distance (e) spatial P_{20} plotted using box-counting (f) spatial P_{21} plotted using box-counting

https://doi.org/10.5194/se-2021-45
Preprint. Discussion started: 21 April 2021

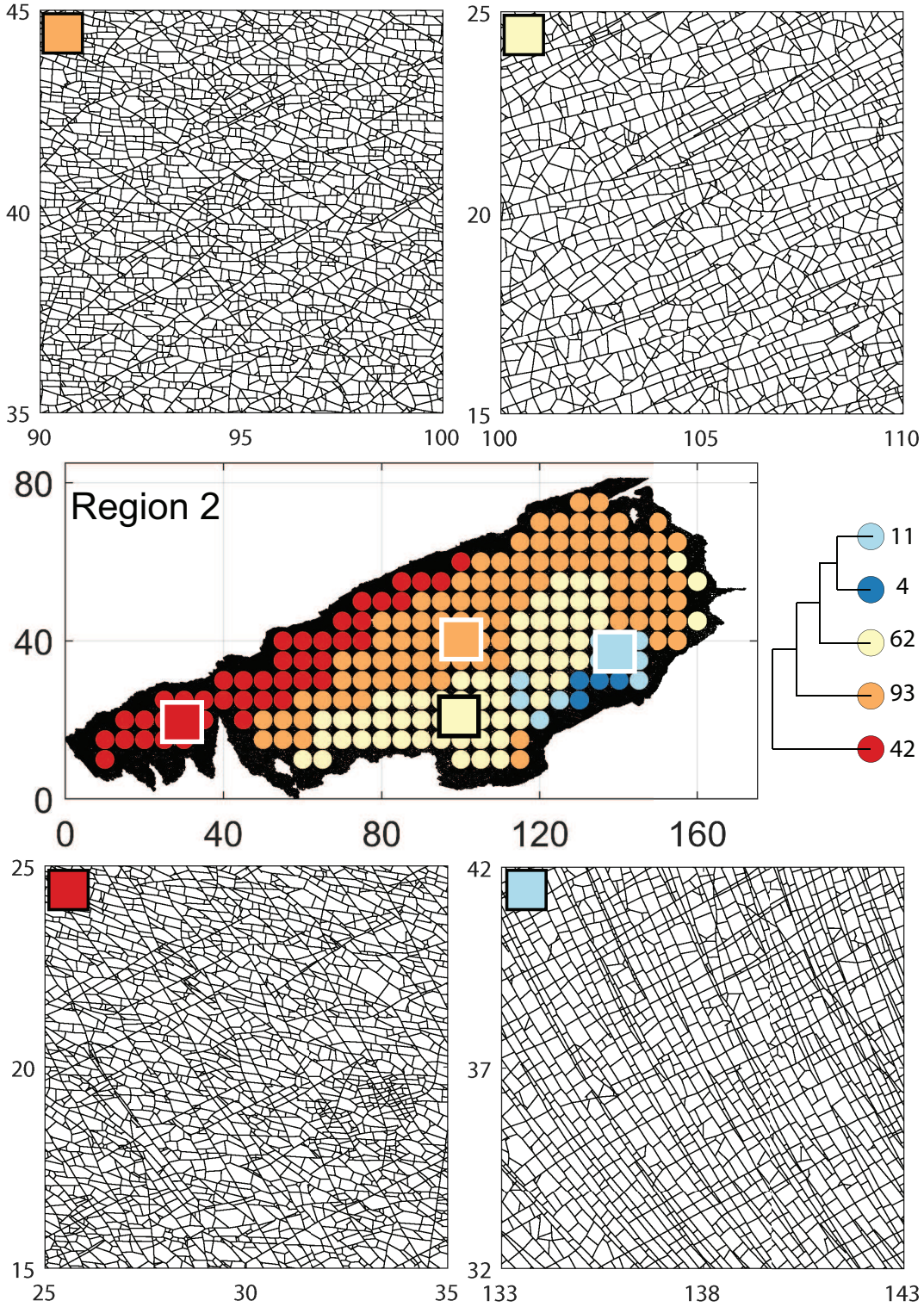

Figure 15. 10 m x 10 m samples depicting variation in fracturing style as identified in the largest four clusters by the fingerprint distance in Region 2

https://doi.org/10.5194/se-2021-45
Preprint. Discussion started: 21 April 2021

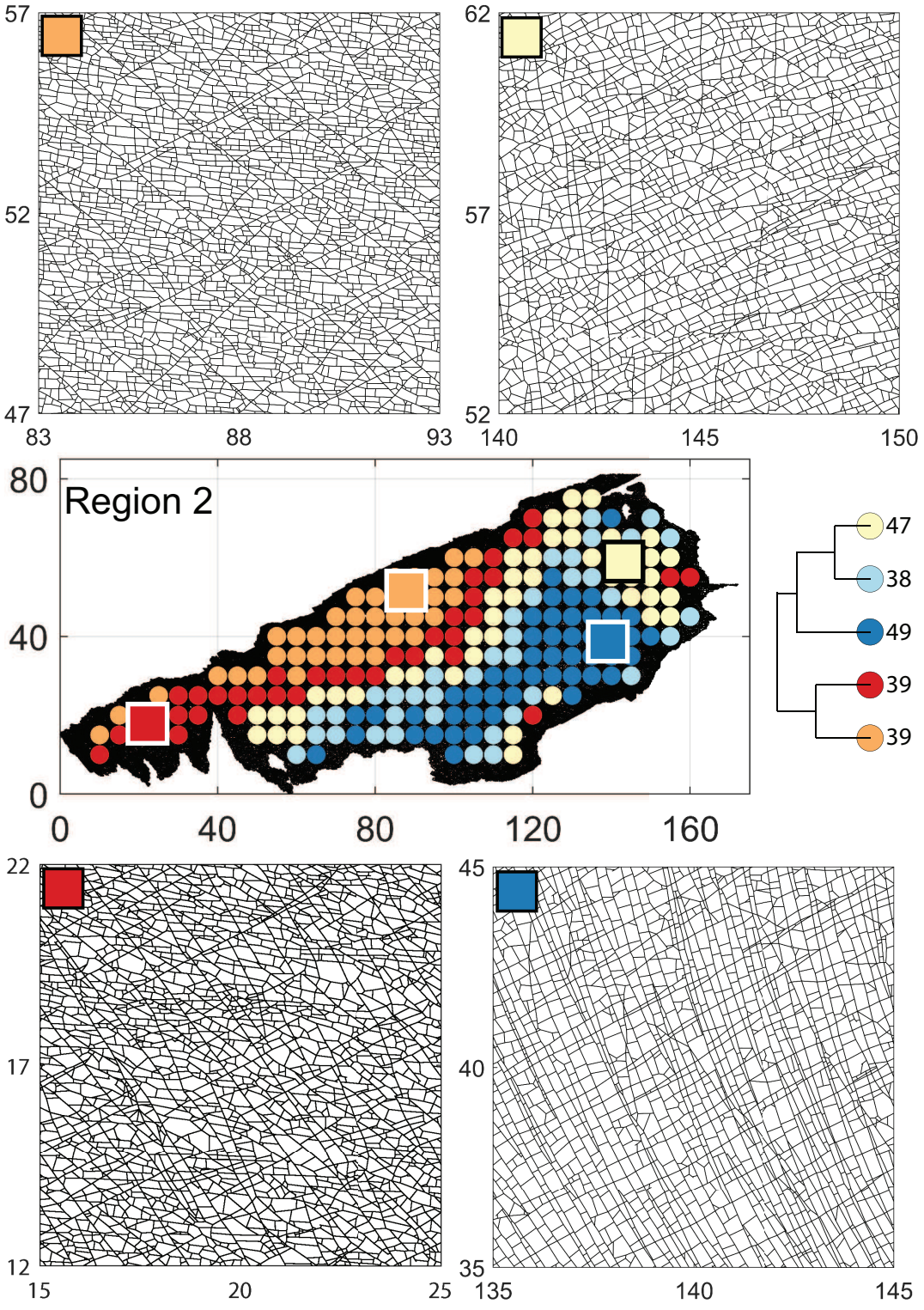

Figure 16. 10 m x 10 m samples depicting variation in fracturing style as identified in the largest four clusters by the D-measure distance in Region 2

https://doi.org/10.5194/se-2021-45
Preprint. Discussion started: 21 April 2021

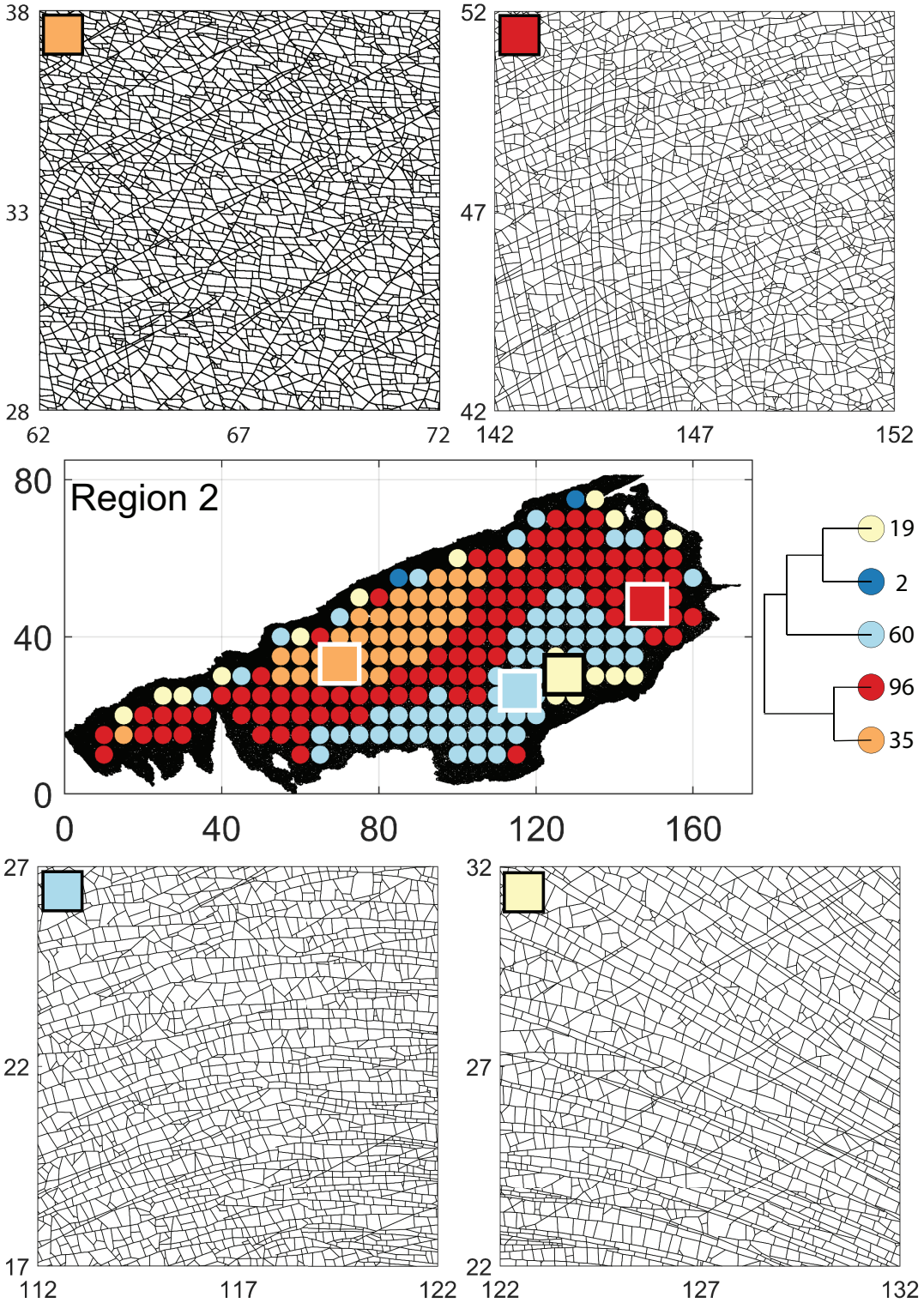

Figure 17. 10 m x 10 m samples depicting variation in fracturing style as identified in the largest four clusters by the portrait divergence distance in Region 2

https://doi.org/10.5194/se-2021-45
Preprint. Discussion started: 21 April 2021

5.3 Region 3

Figure. 18 depicts the heatmap and dendrogram results for Region 3. For all the distance measures, there are clearly discernable clusters from the dendrograms. Figure. 19 depicts the clusters spatially and Table 5 tabulates the corresponding subgraphs. In general, there is a spatial variation in the fracturing in E-W direction as is observable from clustering results of FP, DM, and PD distances. Similar to the Regions 1 and 2, the NetLSD distance results in a speckled pattern where spatial autocorrelation is uncertain.

Table 5. Summary of sub-graphs within each cluster of Region 3

Metric →	FP	DM	LSD	PD
Cluster 1	38	45	44	41
Cluster 2	33	37	38	30
Cluster 3	29	24	16	26
Cluster 4	15	10	10	14
Cluster 5	2	1	9	6
Total			117	

Clustering results from the FP distance is depicted in Fig. 20 with 10 x 10 m cutouts from each sub-region depicting differences in fracturing style corresponding to the top four clusters. The western grouping (in red) contains long, curved fractures that strike NW-SE. This pattern changes as we move east to the adjacent cluster (in orange) where long fractures begin to trend NE-SW. The central region of Region 3 has a different fracturing motif with longer fractures now trending E-N-E (in yellow). At the eastern extremity of Region 3, the long fractures are striking E-W.

Similarly, Fig. 21 depicts 10 x 10 m samplings from clusters identified by the D-Measure distance within Region 3. Overall, the pattern variation is that of a large grouping in the western sub-region (in orange), and a smaller one in the extremities of both east and west (in red). The central region contains a cluster (in light blue) that is flanked on either end by a cluster in yellow. The zoomed-in samples depicts the gradual transition from long fractures striking to the NW-SE in the western end to long fractures striking E-W.

The clusters identified by the PD also show an E-W transition in fracturing (see Fig. 22) as is evident from extracted samples. In the western region, similar to the result of FP distance, there are two clusters (in yellow and orange). Moving eastwards, there is a clearly demarcated central region (dark and light blue) after which the orange cluster repeats itself in the eastern boundary. Comparing with the fracture persistence maps in Fig. 19(e) and Fig. 19(f), the PD clustering seem to be able to differentiate out regions of high fracturing density (dark blue).

https://doi.org/10.5194/se-2021-45
Preprint. Discussion started: 21 April 2021

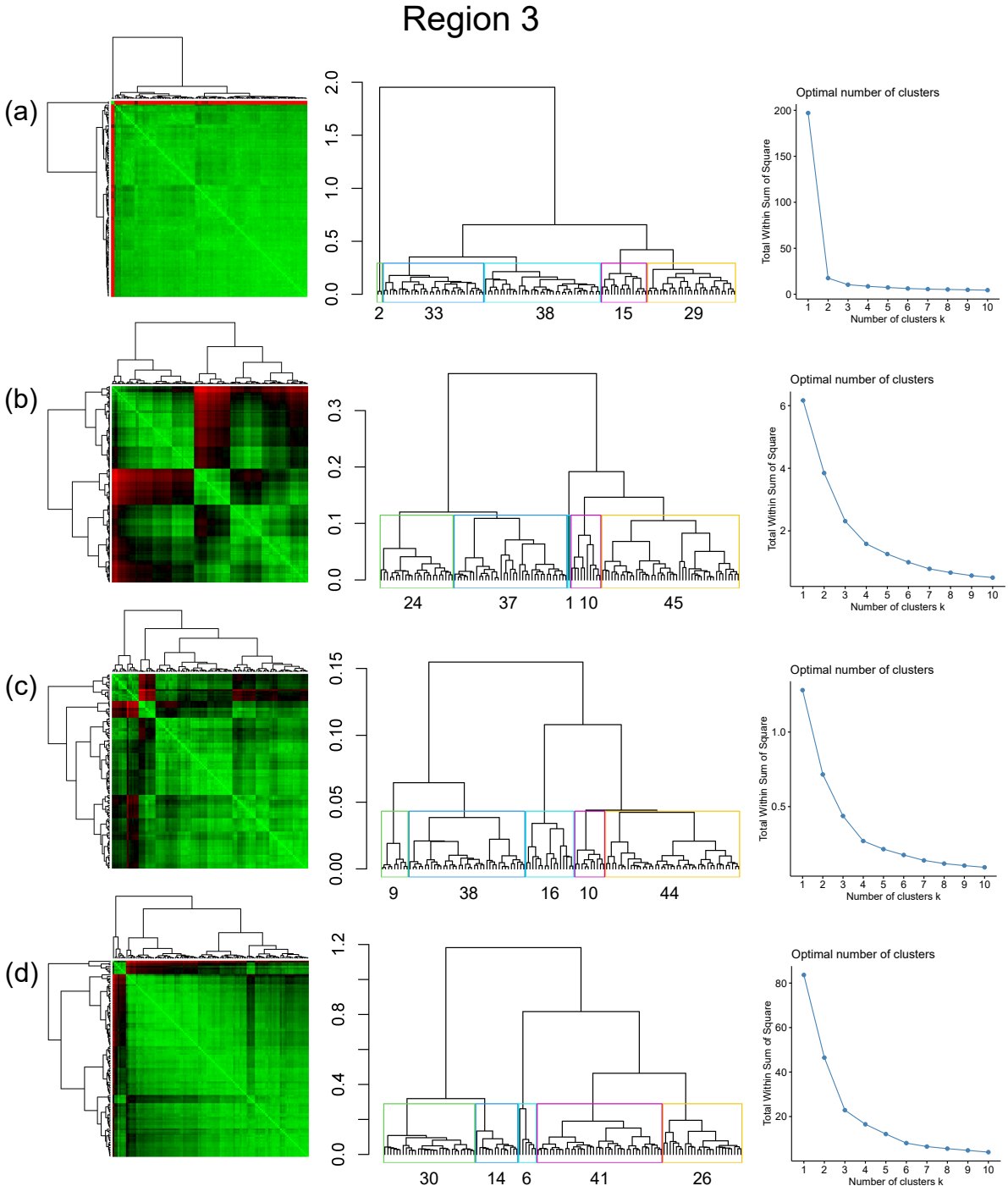

Figure 18. (left) Combined symmetric heatmap of distance matrix and dendrogram for all four distance metrics (centre) enlarged dendrogram depicting height at which the top clusters are extracted (right) weight sum of squares of distances depicting possible number of clusters (FP-Fingerprint, DM-D-measure, LSD-NetLSD, PD-Portrait Divergence)

https://doi.org/10.5194/se-2021-45
Preprint. Discussion started: 21 April 2021

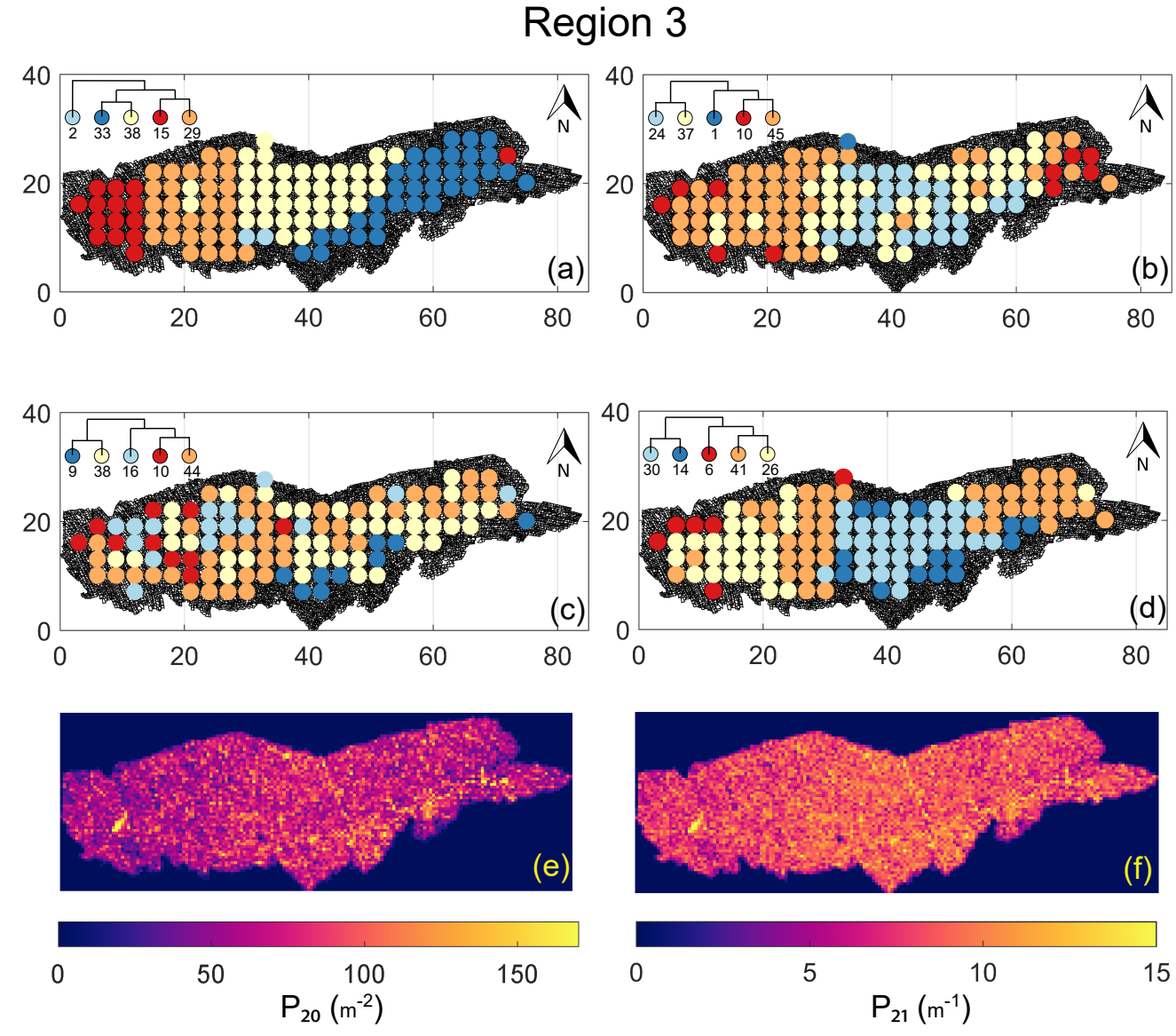

Figure 19. Region 3 hierarchical clustering results (a) clusters computed using fingerprint distance (b) clusters computed using D-measure distance (c) clusters computed using NetLSD distance (d) clusters computed using Portrait Divergence distance (e) spatial P_{20} plotted using box-counting (f) spatial P_{21} plotted using box-counting

https://doi.org/10.5194/se-2021-45
Preprint. Discussion started: 21 April 2021

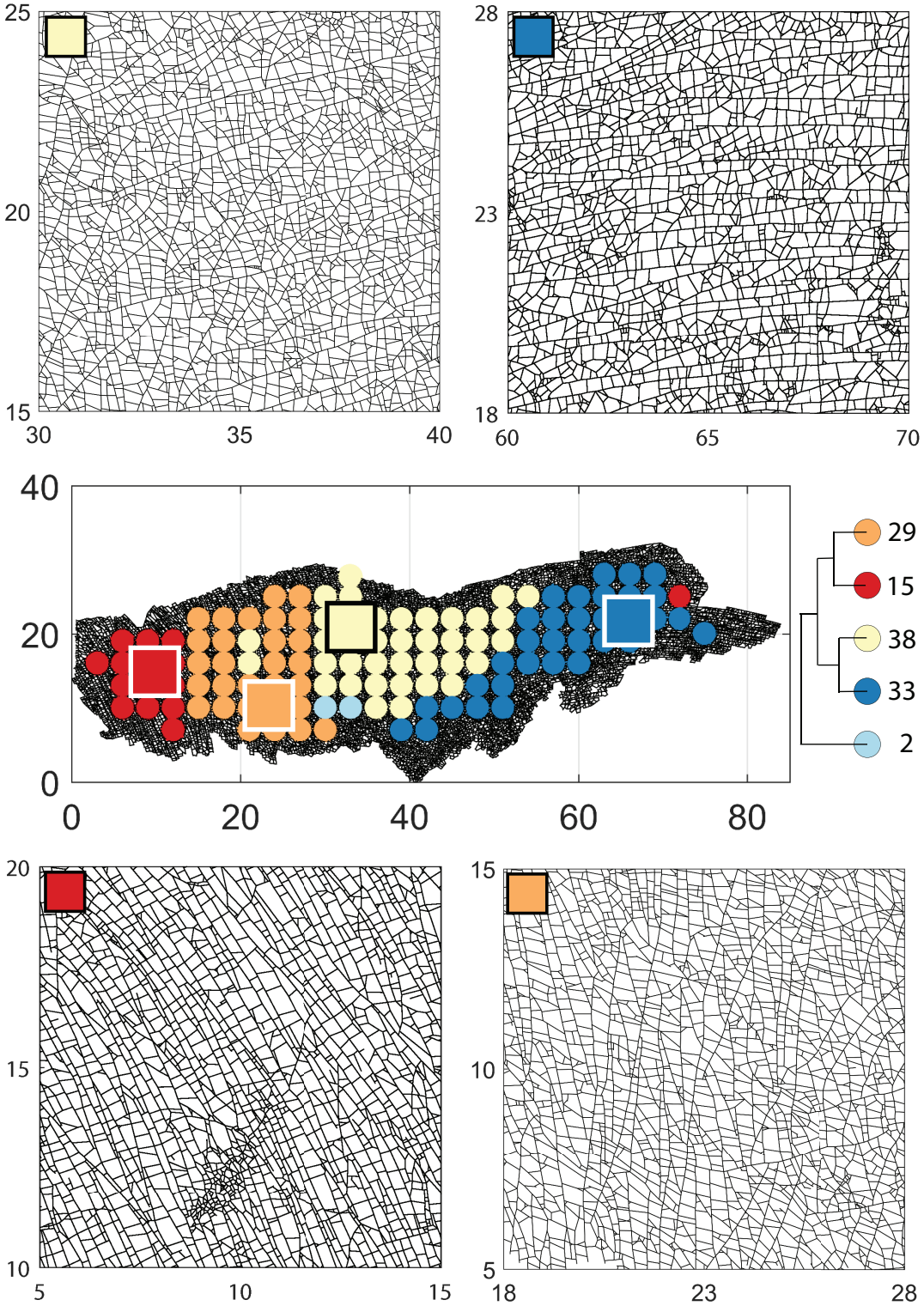

Figure 20. 10 m x 10 m samples depicting variation in fracturing style as identified in the largest four clusters by the fingerprint distance in Region 3

https://doi.org/10.5194/se-2021-45
Preprint. Discussion started: 21 April 2021

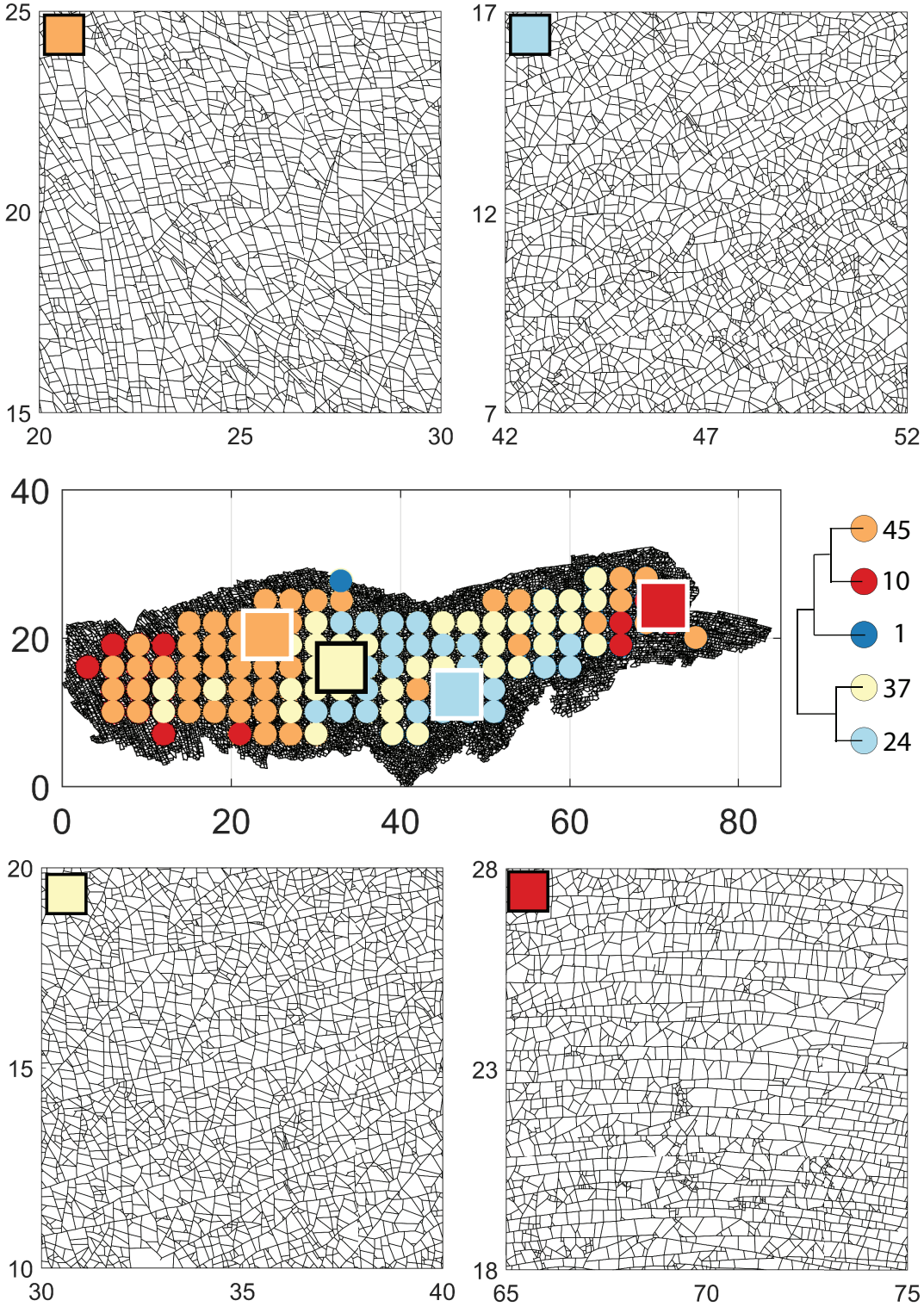

Figure 21. 10 m x 10 m samples depicting variation in fracturing style as identified in the largest four clusters by the D-measure distance in Region 3

https://doi.org/10.5194/se-2021-45
Preprint. Discussion started: 21 April 2021

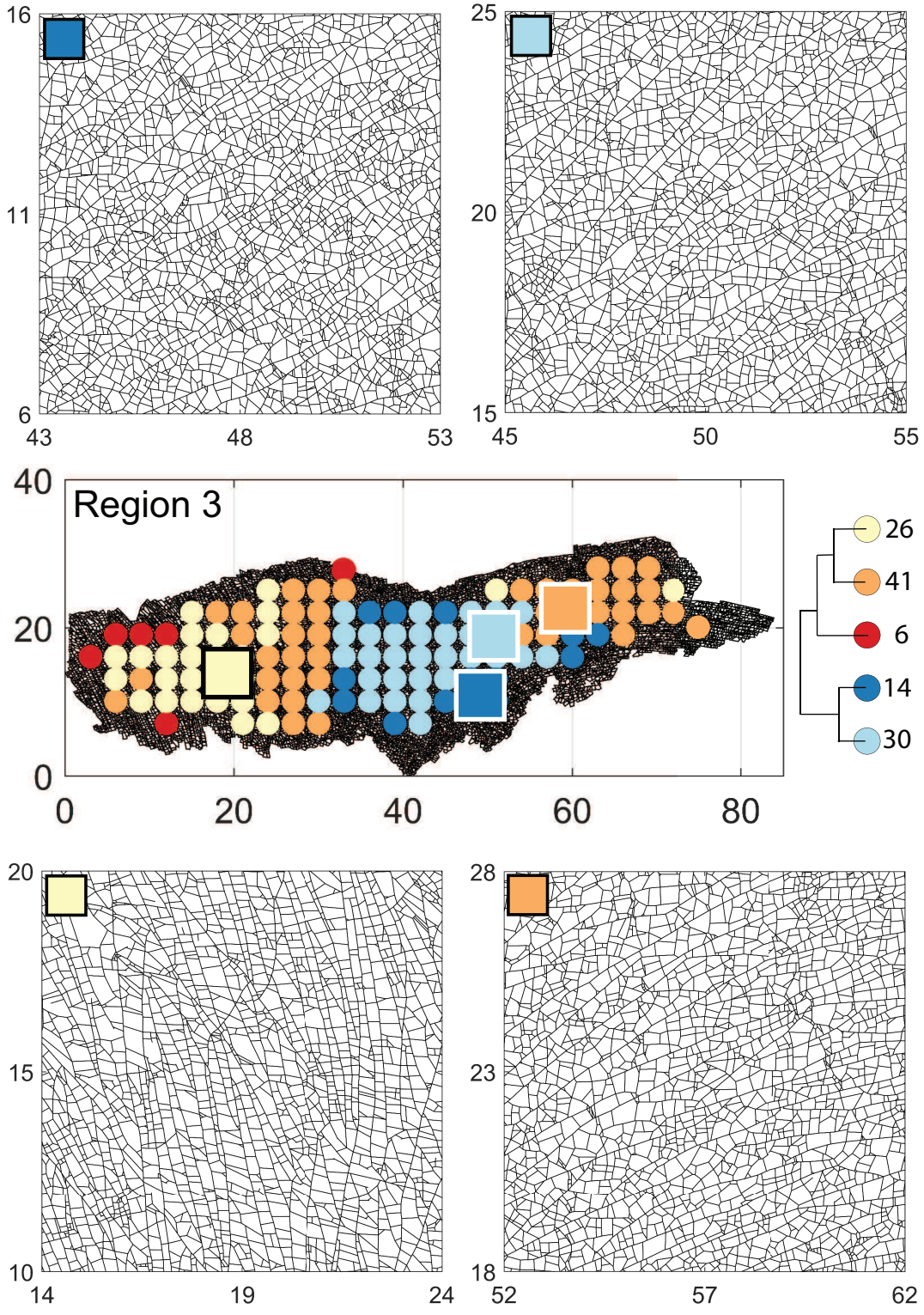

Figure 22. 10 m x 10 m samples depicting variation in fracturing style as identified in the largest four clusters by the portrait divergence distance in Region 3

https://doi.org/10.5194/se-2021-45
Preprint. Discussion started: 21 April 2021

6 Discussion

Within the structural geology literature, the quantitative fracture persistence measures of Dershowitz and Herda (1992), the topological approach of Sanderson and Nixon (2015), and qualitative descriptions are most commonly resorted to for comparing 2D fracture networks. The lack of quantitative measures for spatial network data is partially due to the lack of extensive 2D fracture trace data. Using the fully mapped UAV-derived dataset of a very large fracture set, it is possible to investigate variations in 2D fracture network organization in a systematic manner.

In this contribution, we treat 2D fracture networks as planar graph structures and apply graph similarity measures to quantitatively compare sub-samplings within large fracture networks and discover clusters of similarity. The unsupervised statistical learning technique of HC was used along with graph distance metrics to extract spatial clusters. Sub-graphs within a spatial cluster are more similar to each other than other clusters. A hierarchy of patterns are derived based on similarity scores and these can be examined at deeper levels.

One can argue that variation exists at multiple length scales, and more granular inquiry would lead to different clusters. While our choices of grid-spacing and sub-sampling of graphs were to keep computational requirements in mind, it is possible to do more dense sub-sampling than what we have already achieved to highlight spatial variations within a given network further. The clusters that we have depicted are particular to the spacing and sampling diameters that we have chosen. In this section, we discuss some additional perspectives and issues related to our methodology and results.

– **Linking spatial variation patterns to fracturing drivers** The results indicate that spatial variation in fracture networks is not always obvious from the ubiquitously used fracture persistence measures, such as P_{20} and P_{21}. The proposed method highlights variations in network structure which can then help draw inferences into possible drivers for the spatial differences. In the case of Regions 2 and 3, the proximity to the fault influences network development. Such a model has been proposed by Peacock and Sanderson (1995), Gillespie et al. (2011), and Wyller (2019) where the oldest fractures are long and radial emanating from local asperities within the fault. These older fractures then influence the development of younger fractures. This is observed in Region 2, where clusters form roughly parallel to the E-N-E trending fault with direction of variation to the N-W. Region 3 is positioned between two such asperity epicentres. There are long, radial fractures on the eastern and western extremities with a transition region in-between. The direction of cluster variation trends E-W. Region 1 is not affected by faulting and the network differences can be interpreted as background-variation. Since Regions 1 and 2, pertain to a single layer, the N-E regions of Region 1 show visual similarities between the westernmost extremities of Region 2. The intraregional variations in Region 1 could be due to layer thickness variation although we do not have sufficient thickness data to confirm this.

  The analysis of spatial variation can assist in deciphering fracture timing. Given the temporal nature of network formation, it is desirable to delineate network evolution into relative episodes of fracturing. In previous analyses specific to the Lilstock dataset used in this contribution, Passchier et al. (2021) identified jointing sets with timing history based on fracture length, strike, and topological relationships. Although the temporal history is identified from joints that were picked manually but not fully by Passchier et al. (2021), there is still a discernable spatial variation where some jointing

https://doi.org/10.5194/se-2021-45
Preprint. Discussion started: 21 April 2021

sets are localized while others occur throughout the outcrop. Identifying spatial clustering in complete networks provides a basis by which joint sets can then be arranged in a hierarchy of temporal development.

– **On the choice of a graph distance metric** We have restricted our investigation scope to four state-of-the-art graph similarity distances from the recent graph theory literature. Many more graph distances applicable to spatial graphs exist (Hartle et al., 2020; Tantardini et al., 2019), and the best means remains an open problem in network science research. Some novel distance measures are not graph-based but derive from persistent homology (such as Feng, 2020). In this approach that considers the *shape of data*, persistence diagrams are generated from spatial graphs, and bottleneck distances are used in combination with hierarchical clustering to discover clusters. The results from Feng (2020) compared favourably to that of Louf and Barthelemy (2014) when applied to patterns of cities.

  As may be observed from our results, the metrics highlight certain aspects of the fracture network while not considering others. For instance, the fingerprint distance only considers block area and shape factor distributions of the blocks and neglects orientations. The other three distances use graph properties directly, and hence orientation information (or the lack of it) is a consequence of how the spatial graph is defined. We used weighted graphs that incorporate euclidean distance between nodes as edge weights for the similarity computations. However, each edge also has a striking attribute to completely describe its position in 2D space (in the case of 3D, it needs a dip). Ideally, the edge weight should then be a vector, $w = [l, \theta]$ incorporating both lengths, 'l' and orientation, 'θ', but the distance metrics we use do not allow the use of non-scalar weights. Incorporating both length and strike into a single scalar can be done using a normalized dot product, and we will tackle this issue in future work.

– **Do REV's exist for fracture networks** In the context of fractured reservoir modelling, identification of a representative elemental volume (REV) aids continuum-based simulation approaches. However, the complexities of fluid-flow and transport through fractured porous media require an explicit representation of fractures. Given the difficulties associated with obtaining realistic network geometries, stochastic-process-based methods derived from sparse fracture data are commonplace. These methods are often unable to represent inherent non-stationarity in spatial variation (Thovert et al., 2017) and work by Andresen et al. (2013) find that DFNs from nature exhibit disassortativity, which is not a property of generated networks. Other techniques based on multipoint statistics (Bruna et al., 2019b) attempt image-based approaches to modelling non-stationary networks. Estrada and Sheerin (2017) presents a different approach in which DFNs are directly generated as spatial graphs (referred to as *random rectangular graphs*). Such a method can incorporate insights from outcrop-derived NFRs.

  Regardless of the method used to extrapolate, stationariness decisions have to be made based on hard data, and this is where our approach is helpful. We can use outcrop-derived networks to define and delineate stationarity's spatial boundaries and assign a particular type of network with due cognition of the inherent graph structure. Much literature exists on linking fracture patterns to high-deformation drivers such as folding, faulting, and diapirism, with the goal being to identify and correlate appropriate outcrop analogues to particular subsurface conditions. As our clustering results indicate, at the dimensional scales of sampling we have used, Tobler's first law of geography is applicable to

https://doi.org/10.5194/se-2021-45
Preprint. Discussion started: 21 April 2021

fracture networks. A representative network based on network similarity can be derived. The method can be applied to analogues for which data already exists. Further work is however, required to differentiate fluid-flow and transport responses of the identified cluster type.

– **Other clustering methods** We have used a combination of HC and graph distance metrics to delineate regions within a spatial graph and arrange them in a hierarchy of similarities. Within the graph theory literature, there are other non-HC methods based on graph properties such as modularity (Blondel et al., 2008; Traag et al., 2019) or by graph spectral partitioning (Fiedler, 1973; Spielman and Teng, 2007). Recent developments using graph neural networks and graph machine learning include modifications on the concept of modularity (Tsitsulin et al., 2020) and spectral methods (Bianchi et al., 2020) towards the goal of graph partitioning.

7 Conclusions

This contribution presents a method to automatically identify spatial clusters and quantify intra-network spatial variation within 2D fracture networks. We test the technique on 2D trace data from a prominent limestone outcrop within the Lilstock pavements, located off the southern coast of the Bristol Channel, UK. The fracture network data that spans three separate regions and covers over 14200 sq.m is converted to the form of planar graph structures, spatially sampled into sub-graphs, and then compared using four different graph-distance measures. The pair-wise similarities in the form of distance matrices are used to identify spatially-similar regions using the statistical technique of hierarchically clustering. The results obtained by clustering with the four graph-distance measures (fingerprint distance, D-measure, NetLSD, and Portrait Divergence) reveal interesting intra-network spatial similarity patterns that are not easily discernable from existing global or local fracture network descriptors. The spatial autocorrelation is not easily discernable with the NetLSD distance compared to the other methods. The delineations of these intra-network sub-patterns provide a way to identify representative elemental volumes that preserve fracture networks' topological and geometric properties. The presence of these sub-regions can also serve as a guide to making decisions on stationarity w.r.t geostatistical modelling.

Code and data availability. A MATLAB implementation to compute graph fingerprints and fingerprint distance is available on the Github repository https://github.com/rahulprabhakaran/Fracture_Fingerprint/tree/v.1.0.0 [last access: 19 April 2021; see 10.5281/zenodo.4699961, Prabhakaran (2021)]. The implementation of the D-measure in the form of an R script is available as supplementary code with Schieber et al. (2017). The `NetLSD` python package used to compute the LSD distance as described in Tsitsulin et al. (2018) is available at https://pypi.org/project/NetLSD/. The code implementation for portrait divergence developed by Bagrow and Bollt (2019) can be obtained from https://github.com/bagrow/network-portrait-divergence/.

The circularly sampled fracture subgraphs are derived from the open fracture network dataset published by Prabhakaran (2021). The circularly sampled subgraphs are available for download as a data supplement to this manuscript (Prabhakaran et al., 2021a).

https://doi.org/10.5194/se-2021-45
Preprint. Discussion started: 21 April 2021

Author contributions. RP wrote the code to convert shapefiles to graphs, sample sub-graphs, compute fingerprints and fingerprint distances, did the HC analysis and wrote the manuscript with inputs from all authors. GB and JU contributed to development of methodology, structure of the manuscript and discussion of results. DS provided funding and contributed to discussions on the results and methods that are utilized but are not limited to this manuscript.

Competing interests. The authors declare that they have no known competing financial interests or personal relationships that could have appeared to influence the work reported in this paper.

https://doi.org/10.5194/se-2021-45
Preprint. Discussion started: 21 April 2021

References

Andresen, C., Hansen, A., Le Goc, R., Davy, P., and Hope, S.: Topology of fracture networks, Frontiers in Physics, 1, 7, https://doi.org/10.3389/fphy.2013.00007, 2013.

Bagrow, J. P. and Bollt, E. M.: An information-theoretic, all-scales approach to comparing networks, Applied Network Science, 4, 45, https://doi.org/10.1007/s41109-019-0156-x, 2019.

Bagrow, J. P., Bollt, E. M., Skufca, J. D., and ben Avraham, D.: Portraits of complex networks, EPL (Europhysics Letters), 81, 68 004, https://doi.org/10.1209/0295-5075/81/68004, 2008.

Barthelemy, M.: Morphogenesis of Spatial Networks, Lecture Notes in Morphogenesis, Springer International Publishing, 2018 edn., https://doi.org/10.1007/978-3-319-20565-6, 2018.

Belayneh, M.: Palaeostress orientation inferred from surface morphology of joints on the southern margin of the Bristol Channel Basin, UK, pp. 243–255, 1, Geological Society of London, Special Publications, https://doi.org/10.1144/GSL.SP.2004.231.01.14, https://sp.lyellcollection.org/content/231/1/243, 2004.

Belayneh, M. and Cosgrove, J. W.: Fracture-pattern variations around a major fold and their implications regarding fracture prediction using limited data: an example from the Bristol Channel Basin, Geological Society, London, Special Publications, 231, 89–102, https://doi.org/10.1144/GSL.SP.2004.231.01.06, https://sp.lyellcollection.org/content/231/1/89, 2004.

Bemis, S. P., Micklethwaite, S., Turner, D., James, M. R., Akciz, S., Thiele, S. T., and Bangash, H. A.: Ground-based and UAV-Based photogrammetry: A multi-scale, high-resolution mapping tool for structural geology and paleoseismology, Journal of Structural Geology, 69 (Part A), 163–178, https://doi.org/10.1016/j.jsg.2014.10.007, 2014.

Bianchi, F. M., Grattarola, D., and Alippi, C.: Spectral Clustering with Graph Neural Networks for Graph Pooling, in: Proceedings of the 37th International Conference on Machine Learning, edited by III, H. D. and Singh, A., vol. 119 of *Proceedings of Machine Learning Research*, pp. 874–883, PMLR, http://proceedings.mlr.press/v119/bianchi20a.html, 2020.

Bisdom, K., Nick, H. M., and Bertotti, G.: An integrated workflow for stress and flow modelling using outcrop-derived discrete fracture networks, Computers & Geosciences, 103, 21–35, https://doi.org/10.1016/j.cageo.2017.02.019, 2017.

Bistacchi, A., Mittempergher, S., Martinelli, M., and Storti, F.: On a new robust workflow for the statistical and spatial analysis of fracture data collected with scanlines (or the importance of stationarity), Solid Earth, 11, 2535–2547, https://doi.org/10.5194/se-11-2535-2020, 2020.

Blondel, V. D., Guillaume, J.-L., Lambiotte, R., and Lefebvre, E.: Fast unfolding of communities in large networks, Journal of Statistical Mechanics: Theory and Experiment, 2008, P10 008, https://doi.org/10.1088/1742-5468/2008/10/p10008, 2008.

Bruna, P., Prabhakaran, R., Bertotti, G., Straubhaar, J., Plateaux, R., Maerten, L., Mariethoz, G., and Meda, M.: The MPS-Based Fracture Network Simulation Method: Application to Subsurface Domain, 81st EAGE Conference and Exhibition, London 2019, 2019, 1–5, https://doi.org/10.3997/2214-4609.201901679, 2019a.

Bruna, P.-O., Straubhaar, J., Prabhakaran, R., Bertotti, G., Bisdom, K., Mariethoz, G., and Meda, M.: A new methodology to train fracture network simulation using multiple-point statistics, Solid Earth, 10 (2), 537–559, https://doi.org/10.5194/se-10-537-2019, 2019b.

Dart, C. J., McClay, K., and Hollings, P. N.: 3D analysis of inverted extensional fault systems, southern Bristol Channel basin, UK, Geological Society, London, Special Publications, 88 (1), 393–413, https://doi.org/10.1144/GSL.SP.1995.088.01.21, 1995.

Dershowitz, W. S. and Herda, H. H.: Interpretation of fracture spacing and intensity, in: The 33rd U.S Symposium on Rock Mechanics (USRMS), 3-5 June, Santa Fe, New Mexico, ARMA-92-0757, 1992.

https://doi.org/10.5194/se-2021-45
Preprint. Discussion started: 21 April 2021

Deutsch, C. V.: Geostatistical Reservoir Modeling, Oxford University Press, 1st edition edn., 2002.

Doolaeghe, D., Davy, P., Hyman, J., and Darcel, C.: Graph-based flow modeling approach adapted to multiscale discrete-fracture-network models, PHYSICAL REVIEW E, 102, 53 312, https://doi.org/10.1103/PhysRevE.102.053312, 2020.

Emmert-Streib, F., Dehmer, M., and Shi, Y.: Fifty years of graph matching, network alignment and network comparison, Information Sciences, 346-347, 180 – 197, https://doi.org/10.1016/j.ins.2016.01.074, 2016.

Estrada, E. and Sheerin, M.: Random neighborhood graphs as models of fracture networks on rocks: Structural and dynamical analysis, Applied Mathematics and Computation, 314, 360 – 379, https://doi.org/10.1016/j.amc.2017.06.018, 2017.

Everitt, B., Landau, S., Leese, M., and Stahl, D.: Cluster Analysis, Wiley Series in Probability and Statistics, Wiley, 2011.

Feng, M. H.: Topological tools for understanding complex systems, phdthesis, UCLA, https://doi.org/https://escholarship.org/uc/item/1t32m3z7, https://escholarship.org/uc/item/1t32m3z7, 2020.

Fiedler, M.: Algebraic connectivity of graphs, Czechoslovak Mathematical Journal, 23(2), 298–305, https://doi.org/10.21136/CMJ.1973.101168, 1973.

Gillespie, P., Howard, C., Walsh, J., and Watterson, J.: Measurement and characterisation of spatial distributions of fractures, Tectonophysics, 226, 113 – 141, https://doi.org/10.1016/0040-1951(93)90114-Y, the origin of sedimentary basins: Inferences from quantitative modelling and basin analysis, 1993.

Gillespie, P. A., Monsen, E., Maerten, L., Hunt, D. W., Thurmond, J., and Tuck, D.: Fractures in Carbonates: From Digital Outcrops to Mechanical Models, vol. 10, pp. 137–147, SEPM Society for Sedimentary Geology, 2011 edn., https://doi.org/10.2110/sepmcsp.10.003, 2011.

Hartle, H., Klein, B., McCabe, S., Daniels, A., St-Onge, G., Murphy, C., and Hébert-Dufresne, L.: Network comparison and the within-ensemble graph distance, Proceedings of the Royal Society A: Mathematical, Physical and Engineering Sciences, 476, 20190 744, https://doi.org/10.1098/rspa.2019.0744, 2020.

Hennig, C., Meila, M., Murtagh, F., and Rocci, R.: Handbook of Cluster Analysis, Handbooks of Modern Statistical Methods, Chapman and Hall, CRC Press, 1 edn., 2016.

Jelsma, H. A., de Wit, M. J., Thiart, C., Dirks, P. H. G. M., Viola, G., Basson, I. J., and Anckar, E.: Preferential distribution along transcontinental corridors of kimberlites and related rocks of Southern Africa, South African Journal of Geology, 107, 301–324, https://doi.org/10.2113/107.1-2.301, 2004.

Kaufman, L.: Finding groups in data : an introduction to cluster analysis, Wiley Series in Probability and Statistics, Wiley, New York, 1990 edn., https://doi.org/10.1002/9780470316801, 1990.

Laubach, S. E., Lamarche, J., Gauthier, B. D. M., Dunne, W. M., and Sanderson, D. J.: Spatial arrangement of faults and opening-mode fractures, Journal of Structural Geology, 108, 2–15, https://doi.org/10.1016/j.jsg.2017.08.008, 2018.

Laubach, S. E., Lander, R. H., Criscenti, L. J., Anovitz, L. M., Urai, J. L., Pollyea, R. M., Hooker, J. N., Narr, W., Evans, M. A., Kerisit, S. N., Olson, J. E., Dewers, T., Fisher, D., Bodnar, R., Evans, B., Dove, P., Bonnell, L. M., Marder, M. P., and Pyrak-Nolte, L.: The Role of Chemistry in Fracture Pattern Development and Opportunities to Advance Interpretations of Geological Materials, Reviews of Geophysics, 57, 1065–1111, https://doi.org/10.1029/2019RG000671, 2019.

Lei, Q., Latham, J.-P., Xiang, J., and Tsang, C.-F.: Role of natural fractures in damage evolution around tunnel excavation in fractured rocks, Engineering Geology, 231, 100 – 113, https://doi.org/10.1016/j.enggeo.2017.10.013, 2017.

Louf, R. and Barthelemy, M.: A typology of street patterns, Journal of The Royal Society Interface, 11, 20140 924, https://doi.org/10.1098/rsif.2014.0924, https://royalsocietypublishing.org/doi/abs/10.1098/rsif.2014.0924, 2014.

https://doi.org/10.5194/se-2021-45
Preprint. Discussion started: 21 April 2021

Marrett, R., Gale, J. F., Gómez, L. A., and Laubach, S. E.: Correlation analysis of fracture arrangement in space, Journal of Structural Geology, 108, 16 – 33, https://doi.org/10.1016/j.jsg.2017.06.012, spatial arrangement of fractures and faults, 2018.

Nelson, R.: Geologic Analysis of Naturally Fractured Reservoirs, Gulf Professional Publishing, 2 edn., 2001.

Passchier, M., Passchier, C. W., Weismüller, C., and Urai, J. L.: The joint sets on the Lilstock Benches, UK. Observations based on mapping a full resolution UAV-based image, Journal of Structural Geology, p. 104332, https://doi.org/https://doi.org/10.1016/j.jsg.2021.104332, https://www.sciencedirect.com/science/article/pii/S0191814121000560, 2021.

Peacock, D. and Sanderson, D.: Strike-slip relay ramps, Journal of Structural Geology, 17, 1351 – 1360, https://doi.org/10.1016/0191-8141(95)97303-W, 1995.

Peacock, D., Sanderson, D., and Rotevatn, A.: Relationships between fractures, Journal of Structural Geology, 106, 41 – 53, https://doi.org/10.1016/j.jsg.2017.11.010, 2018.

Prabhakaran, R.: rahulprabhakaran/Fracture-Fingerprint), https://doi.org/10.5281/zenodo.4699961, 2021.

Prabhakaran, R., Bruna, P.-O., Bertotti, G., and Smeulders, D.: An automated fracture trace detection technique using the complex shearlet transform, Solid Earth, 10 (6), 2137–2166, https://doi.org/10.5194/se-10-2137-2019, 2019.

Prabhakaran, R., Bertotti, G., Urai, J., and Smeulders, D.: Data Supplement: Fracture Subgraphs from the Lilstock Pavement, Bristol Channel, UK, 4TU Centre for Research Data. Dataset, https://doi.org/10.4121/14405783.v1, 2021a.

Prabhakaran, R., Urai, J., Bertotti, G., Weismueller, C., and Smeulders, D.: Large-scale natural fracture network patterns: Insights from automated mapping in the Lilstock (Bristol Channel) limestone outcrops, Eartharxiv, https://doi.org/10.31223/X5B61Z, 2021b.

Priest, S. and Hudson, J.: Discontinuity spacings in rock, International Journal of Rock Mechanics and Mining Sciences & Geomechanics Abstracts, 13, 135 – 148, https://doi.org/10.1016/0148-9062(76)90818-4, 1976.

Rawnsley, K., Peacock, D., Rives, T., and Petit, J.-P.: Joints in the Mesozoic sediments around the Bristol Channel Basin, Journal of Structural Geology, 20 (12), 1641–1661, https://doi.org/10.1016/S0191-8141(98)00070-4, 1998.

Sanderson, D. J. and Nixon, C. W.: The use of topology in fracture network characterization, Journal of Structural Geology, 72, 55 – 66, https://doi.org/10.1016/j.jsg.2015.01.005, 2015.

Sanderson, D. J., Peacock, D. C., Nixon, C. W., and Rotevatn, A.: Graph theory and the analysis of fracture networks, Journal of Structural Geology, 125, 155 – 165, https://doi.org/10.1016/j.jsg.2018.04.011, back to the future, 2019.

Schieber, T. A., Carpi, L., Díaz-Guilera, A., Pardalos, P. M., Masoller, C., and Ravetti, M. G.: Quantification of network structural dissimilarities, Nature Communications, 8, 13 928, https://doi.org/10.1038/ncomms13928, 2017.

Spielman, D. A. and Teng, S.-H.: Spectral partitioning works: Planar graphs and finite element meshes, Linear Algebra and its Applications, 421, 284 – 305, https://doi.org/10.1016/j.laa.2006.07.020, special Issue in honor of Miroslav Fiedler, 2007.

Tantardini, M., Ieva, F., Tajoli, L., and Piccardi, C.: Comparing methods for comparing networks, Scientific Reports, 9, 17 557, https://doi.org/10.1038/s41598-019-53708-y, 2019.

Thovert, J.-F., Mourzenko, V., and Adler, P.: Percolation in three-dimensional fracture networks for arbitrary size and shape distributions, Physical Review E, 95 (4), 042 112, https://doi.org/10.1103/PhysRevE.95.042112, 2017.

Traag, V. A., Waltman, L., and van Eck, N. J.: From Louvain to Leiden: guaranteeing well-connected communities, Scientific Reports, 9, 5233, https://doi.org/10.1038/s41598-019-41695-z, 2019.

Tsitsulin, A., Mottin, D., Karras, P., Bronstein, A., and Müller, E.: NetLSD: Hearing the Shape of a Graph, in: Proceedings of the 24th ACM SIGKDD International Conference on Knowledge Discovery and Data Mining, KDD '18, 2018.

Tsitsulin, A., Palowitch, J., Perozzi, B., and Müller, E.: Graph Clustering with Graph Neural Networks, 2020.

https://doi.org/10.5194/se-2021-45
Preprint. Discussion started: 21 April 2021

Valentini, L., Perugini, D., and Poli, G.: The "small-world" topology of rock fracture networks, Physica A: Statistical Mechanics and its Applications, 377, 323 – 328, https://doi.org/10.1016/j.physa.2006.11.025, 2007.

Vevatne, J. N., Rimstad, E., Hope, S. M., Korsnes, R., and Hansen, A.: Fracture networks in sea ice, Frontiers in Physics, 2, 21, https://doi.org/10.3389/fphy.2014.00021, 2014.

Vidal, J., Genter, A., and Chopin, F.: Permeable fracture zones in the hard rocks of the geothermal reservoir at Rittershoffen, France, Journal of Geophysical Research: Solid Earth, 122, 4864–4887, https://doi.org/10.1002/2017JB014331, 2017.

Wang, J. S. Y. and Hudson, J. A.: Fracture Flow and Underground Research Laboratories for Nuclear Waste Disposal and Physics Experiments, chap. 2, pp. 19–41, American Geophysical Union (AGU), https://doi.org/10.1002/9781118877517.ch2, 2015.

Weismüller, C., Passchier, M., Urai, J., and Reicherter, K.: The fracture network in the Lilstock pavement, Bristol Channel, UK: digital elevation models and orthorectified mosaics created from unmanned aerial vehicle imagery, RWTH Publications, https://doi.org/10.18154/RWTH-2020-06903, 2020.

Weismüller, C., Prabhakaran, R., Passchier, M., Urai, J. L., Bertotti, G., and Reicherter, K.: Mapping the fracture network in the Lilstock pavement, Bristol Channel, UK: manual versus automatic, Solid Earth, 11 (5), 1773–1802, https://doi.org/10.5194/se-11-1773-2020, 2020.

Whitaker, A. E. and Engelder, T.: Characterizing stress fields in the upper crust using joint orientation distributions, Journal of Structural Geology, 27, 1778 – 1787, https://doi.org/10.1016/j.jsg.2005.05.016, 2005.

Wierzchoń, S. and Kłopotek, M.: Modern Algorithms of Cluster Analysis, vol. 34 of *Studies in Big Data*, Springer International Publishing, 1 edn., https://doi.org/10.1007/978-3-319-69308-8, 2018.

Witherspoon, P. A.: Flow of groundwater in fractured rocks, Bulletin of the International Association of Engineering Geology - Bulletin de l'Association Internationale de Géologie de l'Ingénieur, 34, 103–115, https://doi.org/10.1007/BF02590241, 1986.

Wyller, F. A.: Spatio-temporal development of a joint network and its properties: a case study from Lilstock, UK, MSc Thesis, 2019.